

Engineering Applications of Computational Fluid Mechanics

ISSN: 1994-2060 (Print) 1997-003X (Online) Journal homepage: www.tandfonline.com/journals/tcfm20

Numerical simulations of the aerodynamic response of circular segments with different corner angles by means of 2D URANS. Impact of turbulence modeling approaches

M. Cid Montoya, F. Nieto, A. J. Álvarez, S. Hernández, J. Á. Jurado & R. Sánchez

To cite this article: M. Cid Montoya, F. Nieto, A. J. Álvarez, S. Hernández, J. Á. Jurado & R. Sánchez (2018) Numerical simulations of the aerodynamic response of circular segments with different corner angles by means of 2D URANS. Impact of turbulence modeling approaches, *Engineering Applications of Computational Fluid Mechanics*, 12:1, 750-779, DOI: [10.1080/19942060.2018.1520741](https://doi.org/10.1080/19942060.2018.1520741)

To link to this article: <https://doi.org/10.1080/19942060.2018.1520741>



© 2018 The Author(s). Published by Informa UK Limited, trading as Taylor & Francis Group



Published online: 10 Oct 2018.



[Submit your article to this journal](#)



Article views: 1764



[View related articles](#)




[View Crossmark data](#)



Citing articles: 1 [View citing articles](#)

Numerical simulations of the aerodynamic response of circular segments with different corner angles by means of 2D URANS. Impact of turbulence modeling approaches

M. Cid Montoya , F. Nieto, A. J. Álvarez, S. Hernández, J. Á. Jurado and R. Sánchez

Structural Mechanics Group, School of Civil Engineering, University of La Coruña, La Coruña, Spain

ABSTRACT

This paper presents the results of numerical and experimental investigations on the force coefficients and Strouhal numbers of circular segments considering different corner angles or chord to sagitta ratios. The research is motivated because these geometries are becoming increasingly popular in several engineering disciplines. The so-called D-section (semi-circular cylinder with a corner angle of 90°) has been experimentally studied in the past, since it is a galloping prone geometry. However, there is a lack of research for cases with different corner angles, and the numerical investigations related to this topic are particularly scarce. In this work, a 2D Unsteady Reynolds Averaged Navier–Stokes approach has been adopted aiming to study the circular segments at the sub-critical regime, considering corner angles from 40° to 90° , and the flow parallel to the rectilinear side. These sections were found to be particularly challenging since they present massive flow separation on the rectilinear side, alongside the inherent difficulties related to modeling the flow along curved surfaces at high Reynolds numbers. The impact of introducing low-Reynolds-number and curvature corrections in the $k - \omega$ SST turbulence model and the performance of the Transition SST model have been extensively studied.

ARTICLE HISTORY

Received 24 December 2017
Accepted 4 September 2018

KEYWORDS

Bluff body aerodynamics; CFD; URANS; turbulence models; circular segment cylinders; wind tunnel tests; sectional models

1. Introduction

Fundamental studies on the aerodynamic response of basic geometries such as circular cylinders (Choi, Jeon, & Kim, 2008; Sumner, 2010; Williamson, 1996; Zdravkovich, 1997, 2003; Zhang, Katsuchi, Zhou, Yamada, & Han, 2016) and rectangular cylinders (Bruno, Coste, & Fransos, 2012; Bruno, Salvetti, & Ricciardelli, 2014; Mariotti, Salvetti, Shoeibi Omrani, & Witteveen, 2016; Patruno, 2015; Ricci, Patruno, de Miranda, & Ubertini, 2016) have been a milestone in the foundation of the experimental fluid mechanics discipline, and more recently in the development of the computational approaches. Furthermore, these basic geometries can be recognized in the built environment such as in buildings or structural members (rectangular cylinders), as well as in power lines, stays in cable supported bridges, chimneys, mooring cables or high-rise buildings (circular cylinders). However, in recent years, new engineering problems in very different fields, and the introduction of certain non-conventional shapes in construction projects have demanded the analysis of different geometries, that have not been so extensively studied in the past. Circular segment geometries, whose geometry can be

characterized by their corner angle β or the chord to sagitta ratio B/H (see Figure 1), are a good example of this statement.

The semicircular geometry ($\beta = 90^\circ$) has been traditionally studied aiming to characterize and mitigate the galloping effects in conductor lines. Furthermore, in recent years, in the field of vibration-based energy harvesting, that is the process of transforming ambient and aeroelastic vibrations to a usable form of energy with the objective of developing self-powered electronic devices (Abdelkefi, 2016), semicircular cylinders attached to the end of a piezoelectric beam have been studied as galloping-based aeroelastic energy harvesters. Comprehensive reviews on aeroelastic-based energy harvesting can be found in Abdelkefi (2016) or Rostami and Arman-dei (2017), while some specific references that focus on the galloping excitation of a semicircular geometry for energy harvesting are Abdelkefi, Hajj, and Nayfeh (2013); Abdelkefi, Yan, and Hajj (2014); Barrero-Gil, Alonso, and Sanz-Andres (2010) or Sirohi and Mahadik (2012), amongst several others. Typical Reynolds numbers of these galloping-based energy harvesters are between 10^4 and 10^5 .

CONTACT M. Cid Montoya  miguel.cid.montoya@udc.es

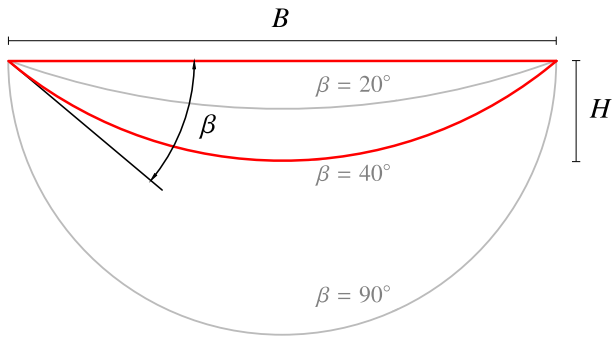


Figure 1. Parametrization of circular segments in terms of width B and corner angle β .

Another relevant problem for framing this piece of research is the study of the gliding performance of the so-called flying snake (*Chrysopelea paradise*). The aerodynamic forces acting on the snake's body, whose cross-section resembles a circular segment, have been studied by means of wind tunnel tests and computational fluid dynamics (CFD) simulations aiming to understand its gliding behavior. A first attempt was conducted by Miklasz and co-workers (Miklasz, LaBarbera, Chen, & Socha, 2010) who studied by means of physical and computational models simplified geometries based on a circular segment, partially or fully filled, considering as corner angle $\beta \approx 60^\circ$, at $Re = 15,000$. As a follow up of the aforementioned study, Holden and co-workers (Holden, Socha, Cardwell, & Vlachos, 2014) adopted a more precise geometry for the snake's body, where the circular segment geometry is slightly modified to resemble a round cornered triangle. In the aforementioned reference, force measurements and particle image velocimetry data were used to analyze the force coefficients, and the wake and vortex shedding characteristics.

If we now turn our attention towards the built environment, circular segments are being increasingly employed nowadays in buildings and bridges. Particularly for footbridges, in recent years a number of realizations have adopted deck cross-sections whose geometries are circular segments such as the Lerez River footbridge in

Spain (Hernández, 1998) (see Figure 2), the Igollo de Camargo footbridge, also in Spain (Pantaleón, Revilla, & Olazábal, 2014), or the Art Institute Footbridge in Chicago (USA) (Algaard, Lewis, Lang, & Johnson, 2010). In the aforementioned realizations, the corner angles of the deck circular segment cross sections, β , range approximately from 33.4° to 84.5° , that correspond to chord to sagitta ratios B/H between 6.66 and 2.2, which shows the very different geometries that are being adopted in these engineering projects. Some other examples of cross sections resembling circular segments can be found in high-rise buildings, such as the Bow Building in Calgary, Canada (Peak Aerials, 2016; Stapleton, 2017), the pylon of the Esplanade Riel pedestrian bridge in Winnipeg, Canada (Winnipeg Architecture Foundation, 2017), or the Shanghai Great Theater.

In the above paragraphs, the widespread use of circular segment geometries with an ample range of corner angles (chord to sagitta ratios), in very different engineering problems, has been highlighted. However, no systematic studies concerning the aerodynamic response of circular segments in terms of their corner angle exist in the literature, to the authors' knowledge. Due to its propensity to galloping, a number of references can be found which report the data of wind tunnel experiments aiming to characterize the aerodynamic response of the semicircular geometry ($\beta = 90^\circ$, $B/H = 2.0$), also named as D-section. These studies were mainly conducted between the decades of 1950 and 1970 (Cheers, 1950; Den Hartog, 1932; Harris, 1949; Novak & Tanaka, 1974; Ratkowski, 1963; Richardson & Martuccelli, 1963), reporting data of the force coefficients for a wide range of angles of attack. However, there is a non-negligible scattering among the results when they are compared, as will be discussed in Section 3. Furthermore, CFD simulations of the aerodynamic response of semi-circular geometries at different corner angles are scarce (Ali, Arafa, & Elaraby, 2013). Moreover, for corner angles different from $\beta = 90^\circ$, only the results for the case $\beta = 60^\circ$ have been reported in Miklasz et al. (2010), and for a value of β about 48° in Zhang and Agarwal (2018).



(a) General view of the footbridge.



(b) Deck cross-section with circular segment shape.

Figure 2. Pedestrian crossing over the Lerez river in Pontevedra, Spain. (a) General view of the footbridge and (b) Deck cross-section with circular segment shape.

2. Research scope

The scope of this research work is to study the aerodynamic response of circular segments considering a wide range of corner angles aiming to establish the relationship between the parameter β and the aerodynamic loading. This might be useful at the early stages of engineering projects to estimate the wind induced loads on these geometries. In the cases that are analyzed in this work the reference angle of attack, $\alpha = 0^\circ$, is that where the flow is parallel to the rectilinear side of the circular segment (see Figure 1). This angle of attack is of interest for simulating the aerodynamic response of footbridge decks, the gliding performance of certain animal species or the feasibility of circular segments with different corner angles, attached to the end of a piezoelectric cantilever beam, to act as relatively low-drag energy harvesters under flow-induced motions such as flutter, galloping, vortex-induced vibration or buffeting (Rostami & Armandei, 2017).

The particular orientation considered in this work ($\alpha = 0^\circ$) presents some challenging features for its correct modeling by means of CFD simulations. In fact, it is anticipated that, two very different aerodynamic behaviors are going to take place simultaneously. On one hand, in the vicinity of the rectilinear side of the circular segment it is expected to have a large region of separated flow, with transition to turbulent flow eventually developing within the separated shear layer, and a large unsteady wake behind the body, as it happens in the case of rectangular cylinders (Sohankar, 2008). In this study, different corner angles are considered and therefore the chord to sagitta ratio of the circular segments is going to change. Hence, it is argued that the reattachment of the flow may take place intermittently, permanently, or not at all, over the rectilinear side, depending on the values of the corner angle. On the other hand, over the circular side, the boundary layer may separate under the influence of a pressure gradient, and the point of flow separation depends on the characteristics of the upstream boundary layer and the near wake flow structure (Bearman, 1997). The well described behavior of the laminar boundary layer separating at about 80° from the stagnation line at the sub-critical regime must take place at the Reynolds number considered in this work, $Re = 10^5$. As the Reynolds number increases ($Re \geq 1.5 \cdot 10^5$), and the shear layer increases its turbulent energy or the boundary layer itself undergoes transition, super-critical and trans-critical regimes are reached (Kwok, 1986; Wilcox, 2011). In summary, for the considered geometries two complex aerodynamic behaviors along with their mutual interaction must be simulated: massive flow separation and eventual reattachment on the rectilinear side, and the Reynolds number dependent boundary layer separation

from the circular side of the circular segment. Obviously, in these two responses, which are interdependent, the transition phenomenon plays a key role.

The CFD approach based on 2D URANS simulations has been chosen because it is usually favored in most of the engineering industrial applications due to its appealing balance between computer power demands and accuracy. However, the averaging in conventional RANS procedures eliminates the effects of linear disturbance growth and this makes extremely difficult to simulate the process of transition from laminar to turbulent flow (Di Pasquale, Rona, & Garrett, 2009; Langtry & Menter, 2009). Popular conventional turbulence models employed in URANS simulations, such as $k - \omega$ SST, would predict transition in the boundary layer at a Reynolds number at least one order of magnitude too small (Collie, Gerritsen, & Jackson, 2008; Wilcox, 2006). Hence, the flow regime associated to the boundary layer transition and separation from the curved side could be incorrectly simulated for the Reynolds number adopted here in the analysis cases. This circumstance must be noted because the Reynolds number adopted in this study is close to the end of the sub-critical regime, shortly before reaching the super-critical regime. The chosen $Re_B = 10^5$ (with regards to the width B of the geometry) corresponds to the Reynolds number typically considered in energy harvesting studies (Barrero-Gil et al., 2010), some biology applications (Holden et al., 2014; Miklasz et al., 2010) and the lower range of wind speeds acting on footbridges and other structures.

Bearing in mind the previously noted limitation in the conventional RANS turbulence models such as the $k - \omega$ SST, the transition phenomenon has been initially tackled in the general CFD practice by introducing low Reynolds corrections in the underlying turbulence model. These turbulence models have been calibrated for viscous sub-layer damping and therefore they show difficulties for faithfully simulate the behavior of transitional flows (Langtry & Menter, 2009). Furthermore, low Reynolds number turbulence models are unable to accurately capture other phenomena that play an important role in transition such as streamline curvature (Menter et al., 2006). Hence, rotation and curvature corrections for these models have also been developed aiming to improve their predictive capabilities (Smirnov & Menter, 2009).

The approach described above, based upon correcting the formulation of basic RANS turbulence models, has proved to be unfeasible for dealing with problems whose physics is governed by the transition phenomenon such as the drag crisis of a cylinder or the transition onset location over an airfoil (Langtry et al., 2006). In the above paragraphs, it has been highlighted the remarkable role that transition is expected to play in the aerodynamic

responses of circular segments. Hence, in some of the simulations that are later reported, transition has been specifically tackled by means of an approach that relies on the use of experimental correlations and it is known as Transition SST turbulence model (Langtry et al., 2006; Menter et al., 2006). This turbulence model is based on two transport equations, one for the intermittency and another for the transition onset criterion, in terms of momentum-thickness Reynolds number. This formulation can be implemented into the general RANS formulation, such as the $k - \omega$ SST turbulence model. It must be borne in mind that the physics of the transition process is allocated in the experimental correlations provided to the model (Langtry & Menter, 2009; Langtry et al., 2006; Menter et al., 2006). This model is more complex and computationally expensive than conventional or corrected versions of the $k - \omega$ SST turbulence model; however, it has proved its feasibility and accuracy in different application cases.

In this piece of research, the aerodynamic response of static circular segments considering corner angles $90^\circ \geq \beta \geq 40^\circ$ is studied by means of wind tunnel tests and CFD simulations. The wind tunnel campaign was conducted considering three different geometries ($\beta = 90^\circ, 60^\circ$ and 40°) and angles of attack in the range ($-10^\circ \geq \alpha \geq 10^\circ$) at $Re_B = 10^5$. The purpose of this experimental campaign is the supply of the required data (force coefficients and Strouhal number) for the validation of the 2D unsteady Reynolds Averaged Navier–Stokes (URANS) simulations that constitute the core of the present research. For the computational simulations, six different geometries were studied ($\beta = 90^\circ, 80^\circ, 70^\circ, 60^\circ, 50^\circ$ and 40°) at two different angles of attack $\alpha = 0^\circ$ and 1° at $Re_B = 10^5$. In this way, in addition to the force coefficients and Strouhal number, the slopes of the force coefficients can be obtained and they can be used for studying buffeting, flutter or galloping responses based on the quasi-steady approach, in the frame of aeroelastic-based energy harvesting studies. The selection of 1° as the angle increment to obtain the slopes of the force coefficients at $\alpha = 0^\circ$ is due to the non-linear response of force coefficients as a function of the angle of attack for these geometries, as it will be shown in the review of the state-of-the-art reported in Section 3 and in the experimental and numerical results reported in Sections 5 and 7. Considering a larger angle of attack (longer step size) may provide inaccurate values for the slopes at $\alpha = 0^\circ$. Particularly, it will be shown in the simulations reported in Section 7 that small variations in the angle of attack modify the length of the separation bubble over the recilinear side, as well as the streamline curvature, and consequently the transition process in the shear layer. Furthermore, the interaction of the upper shear layer with

the leeward corner may also be affected since the eventual reattachment point of the upper shear layer changes with the angle of attack, and this may also affect to the turbulence growth over the reattached boundary layer. Additionally, the interaction between the two shears layer is also affected.

We have conducted an initial set of simulations based on the application of the conventional $k - \omega$ SST turbulence model for $\beta = 40^\circ, 50^\circ, 60^\circ, 70^\circ, 80^\circ$ and 90° and $\alpha = 0^\circ$ and 1° . It was found that for certain geometries and angles of attack this CFD results were very different from the available wind tunnel data. Hence, additional simulations introducing low Reynolds (Wilcox, 1993) and-or curvature corrections (Smirnov & Menter, 2008) were conducted. The ability of these simulations to properly predict the aerodynamic response may be qualified as coincidental (Menter et al., 2006), since in some cases they were successful while in some others they failed to predict the aerodynamic response correctly. Consequently, only when the transition phenomenon was explicitly modelled by means of the four equations version of the $k - \omega$ SST turbulence model (Langtry et al., 2006; Menter et al., 2006), the CFD simulations were capable of predicting correct force coefficients results for the cases where the previous turbulence models had failed.

3. State-of-the-art on the aerodynamics of the semicircular ($\beta = 90^\circ$) cross-section

The instability of a semicircular, or D-section, cylinder was firstly described in Lanchester (1907) and studied by Den Hartog (1932), and later by Harris (1949), Cheers (1950), Richardson and Martuccelli (1963), and Ratkowski (1963). The goal of those research works was to study the galloping effects (see for instance, Blevins, 1990 or Naudascher & Rockwell, 1994) of electric power transmission lines by means of experimental methods. In that context, the lift and drag coefficients of the so-called D-section were provided for a wide range of wind incident angles. In Parkinson and Brooks (1961), the aeroelastic instability of this geometry is discussed, and the force coefficients of a short range of attack angles with the straight side perpendicular to the flow are provided. Later, Novak and Tanaka (1974) studied the effects of turbulence on the galloping stability, providing the force coefficients considering smooth flow and also different values of turbulence intensities and turbulence length scales. The work of Weaver and Veljkovic (2005) contributes by studying the flow-induced vibrations of the cantilever blades of mixing vessels that present parabolic and semicircular cross-sections. In the latter reference, the Strouhal number and lift and moment

coefficients are obtained for the whole range of flow incident angles. In addition, a more recent work by Ali et al. (2013), proposes harvesting energy from the galloping excitation of this section, and analyses this geometry by means of CFD techniques. Finally, the work of Nikitas and Macdonald (2014) reviews the results obtained previously in Den Hartog (1932) and Richardson and Martuccelli (1963), among others, and discusses the performance of the quasi-steady theory for a wide range of geometries.

A summary of the experimental data in the aforementioned references is presented in Table 1, where information on the Reynolds number of each experimental campaign and the turbulence characteristics is provided. A comparison of the lift coefficient as a function of the angle of attack α , obtained from some of these references, is shown in Figure 3, where it can be seen that the reported results show a non-negligible scattering, even for results with similar test settings. A similar situation can be found analyzing the drag and moment coefficients. These discrepancies in the force coefficients may be explained by the differences in the incoming flow characteristics, instrumentation, or degree of sharpness

of the models' corner angles, among some other causes. This motivates conducting additional experimental studies of the D-section and two additional corner angles in this research work, to properly validate the numerical simulations that are later reported in Section 7.

4. Formulation

4.1. Force coefficients

The goal of this work is to characterize the aerodynamic behavior of circular segments. With this aim, sections defined by the corner angle β are studied for various angles of attack α obtaining the force coefficients (C_L , C_D and C_M) and the Strouhal number S_t . These are given by

$$C_L = \frac{L}{\frac{1}{2}\rho U^2 B}, \quad C_D = \frac{D}{\frac{1}{2}\rho U^2 B}, \quad C_M = \frac{M}{\frac{1}{2}\rho U^2 B^2}$$

$$\text{and } S_t = \frac{fH}{U}, \quad (1)$$

where L , D and M are the time-averaged lift and drag forces and moment per unit of length, respectively, with the sign criteria indicated in Figure 4. B and H are the

Table 1. Comparison of the test characteristics of the source references depicted in Figure 3.

Source	Test		Turbulence ^T		Incident angle α		Provided data*		
	Method	Re_B	I [%]	L_x/H	Range	Data	C_D	C_M	S_t
Novak and Tanaka (1974) smooth	Exp.	$9.00 \cdot 10^4$	smooth	2	$[-90,90]$	cont.	✓	✓	✗
Novak and Tanaka (1974) turb.	Exp.	$9.00 \cdot 10^4$	11.0 %	2	$[-90,90]$	cont.	✓	✓	✗
Novak and Tanaka (1974) $L_x/H=1$	Exp.	$5.00 \cdot 10^4$	11.0 %	1	$[-90,90]$	cont.	✓	✓	✗
Novak and Tanaka (1974) $L_x/H=2$	Exp.	$5.00 \cdot 10^4$	11.0 %	2	$[-90,90]$	cont.	✓	✓	✗
Ratkowski (1963)	Exp.	$1.03 \cdot 10^4$	–	–	$[-180,0]$	cont.	✓	✗	✗
Weaver and Veljkovic (2005)	Exp.	$1.00 \cdot 10^5$	≤ 1.0 %	–	$[-90,90]$	each 2.5°	✗	✓	✓
Harris (1949)	Exp.	–	–	–	$[-90,0]$	cont.	✓	✗	✗
Cheers (1950)	Exp.	$6.45 \cdot 10^4$	–	–	$[-90,90]$	cont.	✓	✗	✗
Ali et al. (2013)	Num.	$1.03 \cdot 10^4$	5.0 %	0.28	$[-180,0]$	cont.	✓	✗	✗

* The lift coefficient is always reported. The formulation of the force coefficients is provided in Equation (1).

^T I = turbulence intensity; L_x = turbulence length scale; H = section depth; L_x/H = turbulence length scale normalized to the section depth; – = not reported.

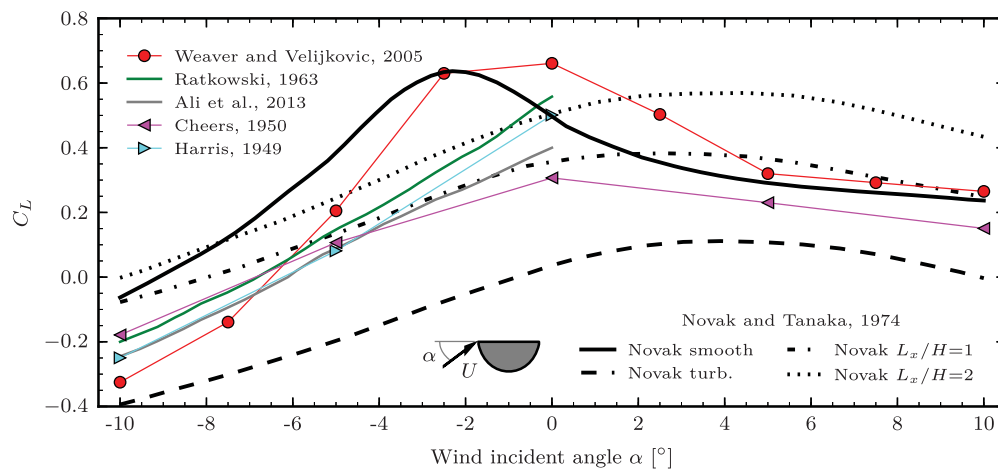


Figure 3. Comparison of the the lift coefficient as a function of the incident angle α for the D-section ($\beta = 90^\circ$) reported by different authors.

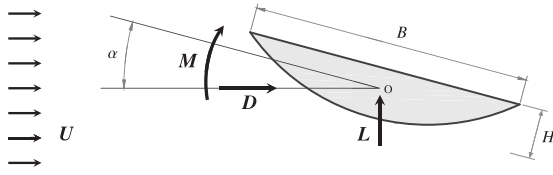


Figure 4. Sign convection adopted for the force coefficients.

chord and the sagitta of the cross-section, U is the wind velocity, ρ is the flow density, and f the vortex shedding frequency.

4.2. URANS governing equations

The numerical assessment of the aerodynamic coefficients is carried out by means of a 2D URANS approach. General description and specific insights about this methodology can be found in Anderson (1995), Wilcox (2005) or Versteeg and Malalasekera (2007) among several others. Although this approach presents some inherent limitations such as the assumptions introduced in the turbulence modeling and the intrinsic perfect correlation of the flow along the span-wise direction that prevents the simulation of 3D flow features, it has demonstrated to be very effective in several engineering disciplines. For instance, in the work by Sun, Owen, and Wright (2009), the performance of the 2D-RANS with regards to its 3D counterpart is analyzed, showing good agreement. In the wind engineering field, some examples of successful application of this approach may be found in the works by Šarkić, Fisch, Höffer, and Bletzinger (2012), Šarkić, Höffer, and Brčić (2015), Nieto, Hargreaves, Owen, and Hernández (2015), Nieto, Owen, Hargreaves, and Hernández (2015), Vairo (2003), Brusiani, de Miranda, Patruno, Ubertini, and Vaona (2013), Chen, Wang, Zhu, and Li (2018), Cid Montoya et al. (2018) or Maruai, Ali, Ismail, and Zaki (2018), among many others. In those works, the performance of 2D URANS to obtain the mean pressure distribution over the cross-sections analyzed and the force coefficients was demonstrated. Furthermore, scale-resolved turbulence models barely improve the quality of these results and drastically increase the computational burden (see the works by Bruno, Fransos, Coste, & Bosco, 2010; Bruno et al., 2012, 2014; Patruno, 2015). Given that the goal of this work is to obtain the force coefficients, the 2D URANS approach is an adequate tool for this task. A brief summary of this approach is outlined below.

The flow around a body in civil engineering applications can be modeled by the URANS equations considering incompressible flow, which means that $\partial\rho/\partial t = 0$, where t represents the time and ρ is the density of the fluid, which is assumed constant in the whole

domain. These equations in conservative form, according to Wilcox (2006), are expressed in tensor notation for the three space dimensions as

$$\frac{\partial U_i}{\partial x_i} = 0, \quad (2)$$

$$\rho \frac{\partial U_i}{\partial t} + \rho U_j \frac{\partial U_i}{\partial x_j} = -\frac{\partial P}{\partial x_i} + \frac{\partial}{\partial x_j} \left(2\mu S_{ij} - \rho \overline{u_i' u_j'} \right), \quad (3)$$

where U_i is the averaged flow velocity vector, u_i' is the fluctuating velocity and $\overline{u_i'}$ its time average, x_i is the position vector, P is the mean pressure, μ is the viscosity of the fluid, and S_{ij} is the mean strain-rate tensor, which is defined as

$$S_{ij} = \frac{1}{2} \left[\frac{\partial u_i}{\partial x_j} + \frac{\partial u_j}{\partial x_i} \right]. \quad (4)$$

The term $-\overline{u_i' u_j'}$ in Equation (3) defines the specific Reynolds stress tensor $\tau_{ij} = -\overline{u_i' u_j'}$, and it is the term that gives place to the closure problem, which is solved by means of turbulence models. One way to face this problem is modeling the Reynolds stress tensor by using the Boussinesq assumption (Wilcox, 2006)

$$\tau_{ij} = 2\nu_T S_{ij} - \frac{2}{3} k \delta_{ij}, \quad (5)$$

where ν_T is the kinematic eddy viscosity and k is the turbulent kinetic energy per unit of mass.

4.3. Turbulence models

The turbulence models based on the Boussinesq assumption (Equation (5)) are named as viscosity models. Some of the most popular viscosity models are the Spalart-Allmaras model (Spalart & Allmaras, 1994), the standard $k - \epsilon$ model (Jones & Launder, 1972; Launder & Sharma, 1974), the RGN $k - \epsilon$ model (Yakhot & Orszag, 1986), Wilcox $k - \omega$ model (Wilcox, 1988) and Menter SST $k - \omega$ model (Menter, 1994; Menter, Kuntz, & Langtry, 2003). A brief summary about them can be found in Xu (2013) for wind engineering applications, particularly in the field of bridge engineering. Comparisons among these models may be found in Hofmann, Kaiser, Kind, and Martin (2007) for applications in the field of jets, or in Tucker (2013) for applications concerning turbomachinery, among others. In this work, several turbulence models and some corrected formulations are used to characterize the aerodynamic behavior of the geometries studied, using the open source code OpenFOAM (Openfoam user guide, 2015) and the ANSYS Fluent (Ansys fluent theory guide, 2013) software. These

turbulence models are described next, and the numerical results are analyzed and discussed by comparing them with wind tunnel experimental data.

4.3.1. Menter's $k - \omega$ SST

This model was first developed by Menter (1994) and improved in Menter and Esch (2001). It is similar to the Wilcox $k - \omega$ turbulence model and includes some refinements from the $k - \epsilon$ model, seeking to take advantage of the robust and accurate formulation of the $k - \omega$ model in the near-wall region and the good performance of the $k - \epsilon$ model in the far field (Wilcox, 2006). This helps to avoid the sensitivity of the results to the freestream values specified for the k and ω . The use of the model in the wind engineering field is widespread, and some interesting applications can be found in Šarkić et al. (2012), Brusiani et al. (2013), de Miranda, Patruno, Ubertini, and Vairo (2014) or Nieto et al. (2015) among many others.

The formulation of this model consists of two transport equations, one for the turbulence kinetic energy k and another for the specific rate of dissipation ω . These are

$$\frac{\partial}{\partial t}(\rho k) + \frac{\partial}{\partial x_i}(\rho k u_i) = \frac{\partial}{\partial x_j} \left(\Gamma_k \frac{\partial k}{\partial x_j} \right) + \tilde{G}_k - \rho \beta^* k \omega, \quad (6)$$

$$\begin{aligned} \frac{\partial}{\partial t}(\rho \omega) + \frac{\partial}{\partial x_i}(\rho \omega u_i) &= \frac{\partial}{\partial x_j} \left(\Gamma_\omega \frac{\partial \omega}{\partial x_j} \right) + G_\omega - \rho \beta \omega^2 \\ &+ 2(1 - F_1) \rho \sigma_{\omega,2} \frac{1}{\omega} \frac{\partial k}{\partial x_j} \frac{\partial \omega}{\partial x_j}, \end{aligned} \quad (7)$$

where Γ_k and Γ_ω are the effective diffusivity of the kinetic energy and the specific rate of dissipation, respectively, G_k and G_ω are the production of turbulence kinetic energy k and dissipation ω , respectively, and μ_t is the turbulent viscosity. These terms are given by

$$\begin{aligned} \Gamma_k &= \mu + \frac{\mu_t}{\sigma_k}, \quad \Gamma_\omega = \mu + \frac{\mu_t}{\sigma_\omega}, \\ \mu_t &= \frac{\rho a_1 k}{\max \left[\frac{\omega a_1}{\tilde{\alpha}^*}, SF_2 \right]}, \end{aligned} \quad (8)$$

$$\begin{aligned} G_\omega &= \frac{\tilde{\alpha}}{\mu_t} G_k, \quad \tilde{G}_k = \min(G_k, \epsilon c_1), \quad \text{and} \\ G_k &= -\overline{\rho u_i' u_j'} \frac{\partial u_j}{\partial x_i}, \end{aligned} \quad (9)$$

where S is the strain-rate magnitude (Equation (4)) and the term ϵc_1 is the production limiter (Menter, 1993), where $\epsilon = \beta^* \rho \omega k$ and c_1 is a constant given in Equation (14). The definition of the eddy viscosity μ_t is the only difference in the formulation of

Menter and Esch (2001) with respect to Menter (1994). Equation (8) presents the version of Menter Esch (2001), while in Menter (1994) vorticity is used instead of the strain-rate S . The terms σ_k and σ_ω are the Prandtl numbers, which can be obtained from

$$\begin{aligned} \sigma_k &= \frac{1}{F_1/\sigma_{k,1} + (1 - F_1)/\sigma_{k,2}} \quad \text{and} \\ \sigma_\omega &= \frac{1}{F_1/\sigma_{\omega,1} + (1 - F_1)/\sigma_{\omega,2}}, \end{aligned} \quad (10)$$

while β and $\tilde{\alpha}$ are blended as

$$\begin{aligned} \beta &= F_1 \beta_1 + (1 - F_1) \beta_2 \quad \text{and} \\ \tilde{\alpha} &= F_1 \tilde{\alpha}_1 + (1 - F_1) \tilde{\alpha}_2, \end{aligned} \quad (11)$$

and the blending functions F_1 and F_2 are obtained from

$$\begin{aligned} F_1 &= \tanh(\Phi_1^4); \\ \Phi_1 &= \min \left[\max \left(\frac{\sqrt{k}}{0.09 \omega y}, \frac{500 \mu}{\rho y^2 \omega} \right), \frac{4 \rho k}{\sigma_{\omega,2} D_\omega^+ y^2} \right]; \quad (12) \\ F_2 &= \tanh(\Phi_2^2); \quad \Phi_2 = \max \left[2 \frac{\sqrt{k}}{0.09 \omega y}, \frac{500 \mu}{\rho y^2 \omega} \right]; \\ D_\omega^+ &= \max \left[2 \rho \frac{1}{\sigma_{\omega,2}} \frac{1}{\omega} \frac{\partial k}{\partial x_j} \frac{\partial \omega}{\partial x_j}, 10^{-10} \right]. \end{aligned} \quad (13)$$

The model relies on dimensional analysis and some closure constants are required. These closure coefficients are chosen by reducing the model to simpler well known cases where relations between the different parameters of the simplified model are known from experimental observations, as described for instance in Wilcox (2006). Thus, the closure coefficients are selected to match these relationships, and in this case they are:

$$\begin{aligned} \sigma_{k,1} &= 1.176, \quad \sigma_{\omega,1} = 0.5, \quad \sigma_{k,2} = 1.0, \\ \sigma_{\omega,2} &= 0.8562, \quad \kappa = 0.41, \quad c_1 = 10, \quad \tilde{\alpha}^* = 1, \\ \tilde{\alpha}_1 &= 0.5532, \quad \tilde{\alpha}_2 = 0.4403, \quad a_1 = 0.31, \\ \beta^* &= 0.09, \quad \beta_1 = 0.075 \quad \text{and} \quad \beta_2 = 0.0828. \end{aligned} \quad (14)$$

4.3.2. Low-Reynolds-number correction

The low-Reynolds-number correction consists of a set of functions that delays the turbulence kinetic energy growth aiming to correct Reynolds-number effects to simulate the gross aspects of transition from laminar to turbulent flow. This correction improves the accuracy when viscous effects are important, and helps to predict the transition from laminar flow into the turbulent flow regime, as described in Wilcox (1992, 2006). This is

carried out by the coefficients $\tilde{\alpha}^*$, $\tilde{\alpha}$ and β^* . The coefficient $\tilde{\alpha}^*$ damps the turbulent viscosity μ_t (Equation (8)) and controls the modeling of the effective diffusivity that determines the transport equations of the $k - \omega$ model, as explained in Wilcox (2006), and can be obtained as

$$\tilde{\alpha}^* = \tilde{\alpha}_\infty^* \left(\frac{\tilde{\alpha}_0^* + Re_T/R_k}{1 + Re_T/R_k} \right), \quad (15)$$

while the coefficient $\tilde{\alpha}$ determines the production of ω in Equation (7), and can be written as

$$\tilde{\alpha} = \frac{\tilde{\alpha}_\infty}{\tilde{\alpha}^*} \left(\frac{\tilde{\alpha}_0 + Re_T/R_\omega}{1 + Re_T/R_\omega} \right), \quad (16)$$

and the coefficient β^* controls the dissipation of k in Equation (6), and is given by

$$\beta^* = \beta_\infty^* \left(\frac{100\beta_0/27 + (Re_T/R_\beta)^4}{1 + (Re_T/R_\beta)^4} \right), \quad (17)$$

where

$$\begin{aligned} Re_T &= \frac{\rho k}{\mu \omega}, \quad R_k = 6, \quad \tilde{\alpha}_0^* = \frac{\beta_i}{3}, \\ \beta_i &= 0.072, \quad \tilde{\alpha}_\infty^* = 1, \quad \tilde{\alpha}_\infty = 0.52, \\ \tilde{\alpha}_0 &= \frac{1}{9}, \quad R_\omega = 2.95, \quad \beta_\infty^* = 0.09, \\ \beta_0 &= 0.0708, \quad \text{and} \quad R_\beta = 8, \end{aligned} \quad (18)$$

being Re_T the turbulence Reynolds number. It must be noted that in high-Reynolds numbers $\tilde{\alpha}^* = 1$. This approach was originally developed for the Wilcox's standard $k - \omega$ model (Wilcox, 1988), and its performance for this model was evaluated in Wilcox (1993) and Wilcox (2006). Since the $k - \omega$ SST model presents the same formulation in the near-wall region as the standard $k - \omega$ model, the implementation of the Low-Reynolds correction is the same. Application examples of this approach in the $k - \omega$ SST model can be found in Vilalpando, Reggio, and Ilinca (2012) and Ghahremanian and Moshfegh (2014), among many others.

4.3.3. Curvature correction

The curvature correction, also known as Spalart-Shur correction, may be applied to the two-equation eddy-viscosity models in order to deal with their insensitivity to streamline curvature and system rotation, which are relevant in turbulent flows, by means of modifying the production term G_k (Equation (9)). It was developed by Smirnov and Menter (2008), although this work is based on the original contributions of Spalart and Shur (1997) and Shur, Strelets, and Travin (2000). The correction is based on the 'rotation function' proposed by Spalart

and Shur, which is an empirical function to account for streamline curvature and system rotation effect. This function can be written as

$$\begin{aligned} f_{\text{rotation}}(r^*, \hat{r}) &= \\ &= (1 + c_{r1}) \frac{2r^*}{1 - r^*} [1 - c_{r2} \tan^{-1}(c_{r2} \hat{r})] - c_{r1}, \end{aligned} \quad (19)$$

where the components \hat{r} and r^* are given by

$$\begin{aligned} \hat{r} &= 2\Omega_{ik}S_{jk} \left[\frac{DS_{ij}}{Dt} + (\epsilon_{imn}S_{jn} + \epsilon_{jmn}S_{in}) \Omega_m^{\text{Rot}} \right] \frac{1}{\hat{D}}, \\ \text{and} \quad r^* &= \frac{S}{\Omega}, \end{aligned} \quad (20)$$

where the strain-rate S and the vorticity tensor Ω can be obtained as

$$\begin{aligned} \Omega^2 &= 2\Omega_{ij}\Omega_{ij}, \quad \Omega_{ij} = \frac{1}{2} \left(\frac{\partial u_i}{\partial x_j} + \frac{\partial u_j}{\partial x_i} \right) + 2\epsilon_{mji}\Omega_m^{\text{rot}}, \\ S^2 &= 2S_{ij}S_{ij} \end{aligned} \quad (21)$$

and Equation (4), and the constants of Equation (19) for the $k - \omega$ SST model are defined in Smirnov and Menter (2008) as $c_{r1} = 1$, $c_{r2} = 2$ and $c_{r3} = 1$. The rotation function f_{rotation} defined in Equation (19) is used to multiply the production term G_k of Equation (9), giving place to $G_k \cdot f_{\text{rotation}}$. The implementation in ANSYS Fluent (Ansys fluent theory guide, 2013) sets limits to the values of the rotation function, from 0 to 1.25. These values represent, for instance, a strong convex curvature without turbulence production in the case $f_{\text{rotation}} = 0$, and on the other hand, a strong concave curvature with high turbulence production when $f_{\text{rotation}} = 1.25$.

This formulation has been tested in several recent works comparing the results of the Spalart-Shur correction with other turbulence models. Some recent references can be found in Da Soghe, Innocenti, Andreini, and Poncet (2010), Dhakal and Walters (2011), Ahmad, Proctor, and Perry (2013), Tao, Xiao, Yang, and Wang (2014) and Zhang, Wray, and Agarwal (2016).

4.3.4. Transition SST model

The Transition SST turbulence model was developed by Menter et al. (2006) and Langtry et al. (2006). The goal of this four-equation model is to improve in boundary layers and separation from the transition from laminar to turbulent flow. This model is a modification of the two-equation $k - \omega$ SST coupling two additional transport equations to the original equations of the $k - \omega$ SST model (Equations (6) and (7)). The additional transport equations focus on the intermittency γ and the transition

onset criteria. The first one is given by

$$\begin{aligned} \frac{\partial(\rho\gamma)}{\partial t} + \frac{\partial(\rho U_j \gamma)}{x_j} &= P_{\gamma 1} - E_{\gamma 1} + P_{\gamma 2} - E_{\gamma 2} \\ &+ \frac{\partial}{\partial x_j} \left[\left(\mu + \frac{\mu_t}{\sigma_\gamma} \right) \frac{\partial \gamma}{\partial x_j} \right], \end{aligned} \quad (22)$$

where the transition ($P_{\gamma 1}$ and $E_{\gamma 1}$) and destruction or relaminarization ($P_{\gamma 2}$ and $E_{\gamma 2}$) sources are given by

$$\begin{aligned} P_{\gamma 1} &= C_{a1} F_{\text{length}} \rho S [\gamma F_{\text{onset}}]^{c_{\gamma 3}}, \\ P_{\gamma 2} &= C_{a2} \rho \Omega \gamma F_{\text{turb}}, \\ E_{\gamma 1} &= C_{e1} P_{\gamma 1} \gamma, \quad \text{and} \quad E_{\gamma 2} = C_{e2} P_{\gamma 2} \gamma, \end{aligned} \quad (23)$$

where F_{length} is an empirical correlation that controls the length of the transition region. In addition, the transition onset is driven by

$$\begin{aligned} F_{\text{onset}} &= \max \left(\min \left(\max \left(F_{\text{onset}1}, F_{\text{onset}1}^4, 0 \right), 2.0 \right) \right. \\ &\quad \left. - \max \left(1 - \left(\frac{Re_T}{2.5} \right)^3, 0 \right), 0 \right), \end{aligned} \quad (24)$$

$$\begin{aligned} F_{\text{turb}} &= e^{-\left(\frac{Re_T}{4}\right)^4}, \quad Re_v = \frac{\rho \gamma^2 S}{\mu}, \quad Re_T = \frac{\rho k}{\mu \omega}, \quad \text{and} \\ F_{\text{onset}1} &= \frac{Re_v}{2.193 Re_{\theta_c}}, \end{aligned} \quad (25)$$

where γ is the wall distance and Re_{θ_c} is the critical Reynolds number in which the intermittency first starts to increase in the boundary layer and is given by an empirical correlation. The coefficients for these equations are:

$$\begin{aligned} C_{a1} &= 2, \quad C_{e1} = 1, \quad C_{a2} = 0.06, \quad C_{e2} = 50, \\ C_{\gamma 3} &= 0.5 \quad \text{and} \quad \sigma_\gamma = 1.0. \end{aligned} \quad (26)$$

The transport equations for the transition momentum thickness Reynolds number $R\tilde{e}_{\theta_t}$ can be written as

$$\begin{aligned} \frac{\partial(\rho R\tilde{e}_{\theta_t})}{\partial t} + \frac{\partial(\rho U_j R\tilde{e}_{\theta_t})}{x_j} &= P_{\theta_t} \\ &+ \frac{\partial}{\partial x_j} \left[\sigma_{\theta_t} (\mu + \mu_t) \frac{\partial R\tilde{e}_{\theta_t}}{\partial x_j} \right], \end{aligned} \quad (27)$$

where the source terms of this expression are

$$\begin{aligned} P_{\theta_t} &= c_{\theta_t} \frac{\rho}{t} (Re_{\theta_t} - R\tilde{e}_{\theta_t}) (1.0 - F_{\theta_t}), \\ t &= \frac{500\mu}{\rho U^2}, \quad F_{\text{wake}} = e^{-\left(\frac{Re_\omega}{10^5}\right)^2}, \end{aligned} \quad (28)$$

$$\begin{aligned} F_{\theta_t} &= \min \left(\max \left(F_{\text{wake}} e^{(-\frac{\gamma}{\delta})^4}, 1.0 \right) \right. \\ &\quad \left. - \left(\frac{\gamma - 1/50}{1.0 - 1/50} \right)^2 \right), 1.0 \end{aligned} \quad (29)$$

$$\begin{aligned} \theta_{BL} &= \frac{R\tilde{e}_{\theta_t} \mu}{\rho U}, \quad \delta_{BL} = \frac{15}{2} \theta_{BL}, \quad \delta = \frac{50\Omega \gamma}{U} \delta_{BL}, \quad \text{and} \\ Re_\omega &= \frac{\rho \omega y^2}{\mu}, \end{aligned} \quad (30)$$

and the constants of these equations are $c_{\theta_t} = 0.03$ and $\sigma_{\theta_t} = 2.0$. The boundary conditions for $R\tilde{e}_{\theta_t}$ at a wall is zero flux. The model contains three empirical correlations to define Re_{θ_t} (Equation (28)), Re_{θ_c} (Equation (25)) and F_{length} (Equation (23)), that can be found in detail in Langtry and Menter (2009).

The separation-induced transition correction is implemented as

$$\begin{aligned} \gamma_{\text{sep}} &= \\ &= \min \left(C_{s1} \max \left[\left(\frac{Re_v}{3.235 Re_{\theta_t}} \right) - 1.0 \right] F_{\text{reattch}}, 2 \right) F_{\theta_t} \end{aligned} \quad (31)$$

$$F_{\text{reattch}} = e^{-\left(\frac{Re_T}{20}\right)^2}, \quad \gamma_{\text{eff}} = \max(\gamma, \gamma_{\text{sep}}), \quad (32)$$

where $C_{s1} = 2.0$.

In order to couple the transition model and the SST transport equations, the k -equation is modified as

$$\frac{\partial(\rho k)}{\partial t} + \frac{\partial(\rho k u_i)}{\partial x_i} = \frac{\partial}{\partial x_j} \left(\Gamma_k \frac{\partial k}{\partial x_j} \right) + G_k^* - Y_k^* + S_k \quad (33)$$

$$G_k^* = \gamma_{\text{eff}} \tilde{G}_k, \quad Y_k^* = \min(\max(\gamma_{\text{eff}}, 0.1), 1.0) Y_k, \quad (34)$$

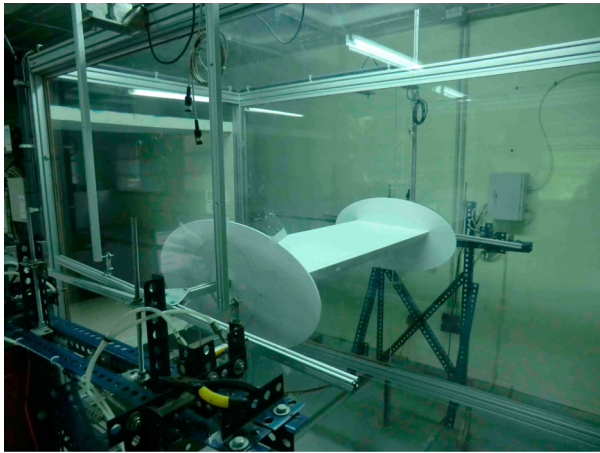
where \tilde{G}_k and Y_k are the original production and destruction terms in the SST $k - \omega$ model.

Some application examples of this turbulence model can be found in the recent works by Grabe (2013) and Lanzafame, Mauro, and Messina (2014).

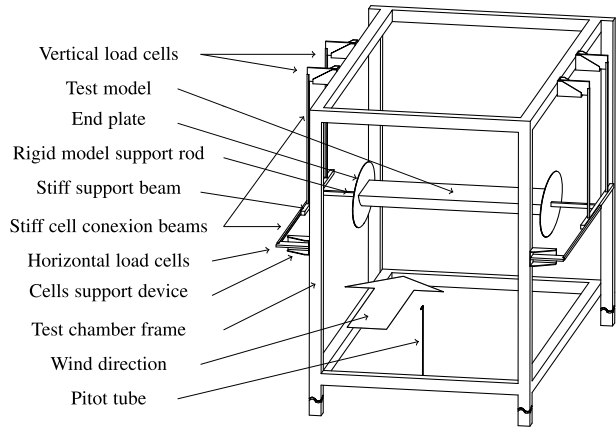
5. Experimental campaign

5.1. Wind tunnel characteristics

Three sectional models of circular segments corresponding to corner angles $\beta = [40^\circ, 60^\circ, 90^\circ]$ have been tested in the aerodynamic wind tunnel of the University of La Coruña. The wind tunnel is an open circuit tunnel with



(a) Experimental test set-up for case $\beta = 60^\circ$.



(b) Suspension and measurement system for aerodynamic tests.

Figure 5. Description of the experimental test set-up and the suspension system. (a) Experimental test set-up for case $\beta = 60^\circ$ and (b) suspension and measurement system for aerodynamic tests.

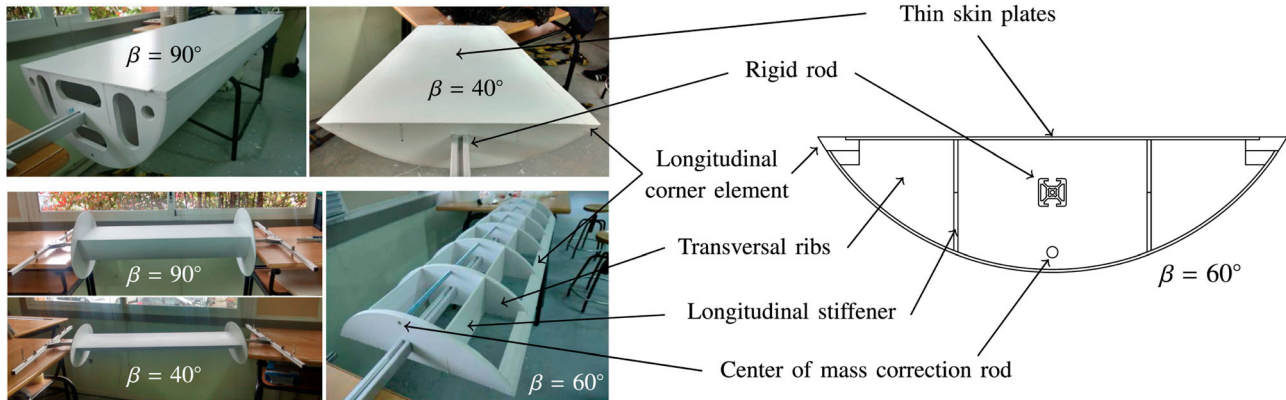


Figure 6. Sectional models for sections $\beta = [40^\circ, 60^\circ, 90^\circ]$, and sectional model elements.

a test chamber of $2 \times 1 \times 1 \text{ m}^3$ in open configuration, which gives place to a test section of $1 \times 1 \text{ m}^2$. This facility reaches velocities up to 30 m/s, achieved with a contraction rate of 6:1 in the nozzle after the flow conditioner. In Figure 5(a), a picture of the sectional model $\beta = 60^\circ$, fitted with elliptic shaped end-plates, inside the test section can be seen. Furthermore, the main components of the experimental set up are identified in Figure 5(b)).

5.2. Sectional models features

The models are 0.97 m long and 0.34 m wide so that the spanwise length to width ratio is close to 3. They were built using aluminum bars to provide internal stiffness by means of a *H*-shaped frame structure and foamed PVC with a density of 0.5 g/cm^3 to reproduce the outside geometry of the model, as sketched in Figure 6. The curved surface of the circular segments is achieved by bending thick foamed PVC plates of 2 mm over the internal curved PVC ribs, 10 mm thick, that define the

geometry of the model. Special care was taken to accurately replicate the desired geometry and guarantee a high degree of sharpness in the corners, given the notable influence of the latter on the results of the force coefficients, as it has been remarked for instance, in Tamura and Miyagi (1999) or Fransos and Bruno (2010). In addition, the surfaces of the models were treated so that they can be considered as smooth surfaces, given that variations in the roughness can lead to strong variations in the measurements, as described in Achenbach Heinecke (1981). Elliptical plates are placed at both sides of the sectional models to avoid 3D effects in those zones.

5.3. Reynolds number sensitivity

The Reynolds-number dependency of the aerodynamic response of circular cylinders is widely known and it has been studied, for instance, in the works of Schewe (1983, 1986). Hence, in order to ascertain the influence of this parameter in the results, a study on the Reynolds number

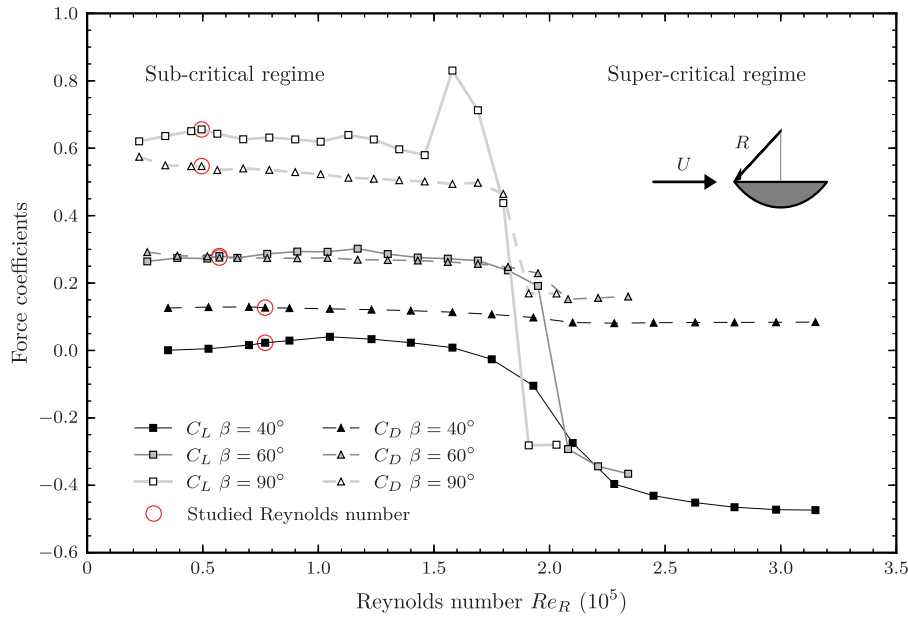


Figure 7. Effect of Reynolds number considering the radius R as characteristic dimension for defining the Reynolds number Re_R .

sensitivity of the three tested models has been carried out. The results are shown in Figure 7, where the drag and lift coefficients of the three models are reported.

Changes in the flow regime in curved shapes are controlled by variations in the location of the flow separation point in the curved side of the geometry (Schewe, 2001). This is the case of circular-based geometries, and given that the three sections under study are circular segments, the Reynolds number effects should eventually occur at similar Reynolds numbers when expressed in terms of a curvature-related dimension. Hence, the results shown in Figure 7 are expressed as a function of the Reynolds number considering as reference dimension the radius of the circular segment (Re_R). It can be seen that the regime change occurs at approximately the same Reynolds number for the three geometries, about $Re_R = 2 \cdot 10^5$. The same behavior is found for a circular cylinder when changing from the sub-critical to the super-critical regimes due to the delay in the separation point, as described for instance in Holmes (2015). This Reynolds number corresponds to Reynolds numbers in terms of the section width B between $2.5 \cdot 10^5$ and $4 \cdot 10^5$ for the three sections considered herein.

It can be also appreciated that there is a significant increase in C_L for the $\beta = 90^\circ$ geometry before the drop associated to the regime change, around $Re_R = 1.5 \cdot 10^5$. This peak in the lift coefficient might be explained by the asymmetric flow separation associated to discontinuous transitions in circular cylinders, that has been identified in Schewe (1983) for Re_R between $1.4 \cdot 10^5$ and $1.75 \cdot 10^5$. These discontinuous transitions cause non-zero steady lift on circular cylinders at a critical Reynolds number

range. When the boundary layer over the curved surface experiences transition from laminar to turbulent, a laminar separation bubble is formed. This may also decelerate the flow over the rectilinear side of the D-section. Further studies on shear layer instability (Singh & Mittal, 2005) and the interaction between shear layers would be required for this cross-section due to the lack of data for non-symmetrical geometries in the flow direction, as it has been highlighted by Bot, Rabaud, Thomas, Lombardi, and Lebret (2016). A similar peak has been described for circular cylinders in smooth flow in terms of C_D in the work by Kwok (1986).

Taking the Reynolds number sensitivity mentioned above into account, the force coefficients and Strouhal number that are going to be reported hereafter have been obtained at ($Re_B = 1 \cdot 10^5$) (in terms of B), which corresponds to a flow speed of 4.4 m/s. At this flow speed the turbulence intensity measured at the inlet of the test chamber is $I = 2\%$, according to the expression reported in Holmes (2015).

5.4. Force coefficients and Strouhal numbers

The wind tunnel results of the force coefficients as a function of the angle of attack are presented in Figure 8 for the three circular segment geometries $\beta = [40^\circ, 60^\circ, 90^\circ]$, where clear differences can be appreciated. The case $\beta = 40^\circ$ is the most streamlined cross-section and the $\beta = 90^\circ$ is the bluffest geometry. For the $\beta = 40^\circ$ geometry, the slope of the lift coefficient is positive and the drop in the C_L appears around $\alpha = 8^\circ$, the drag coefficient is more-or-less uniform, about 0.1, and the moment

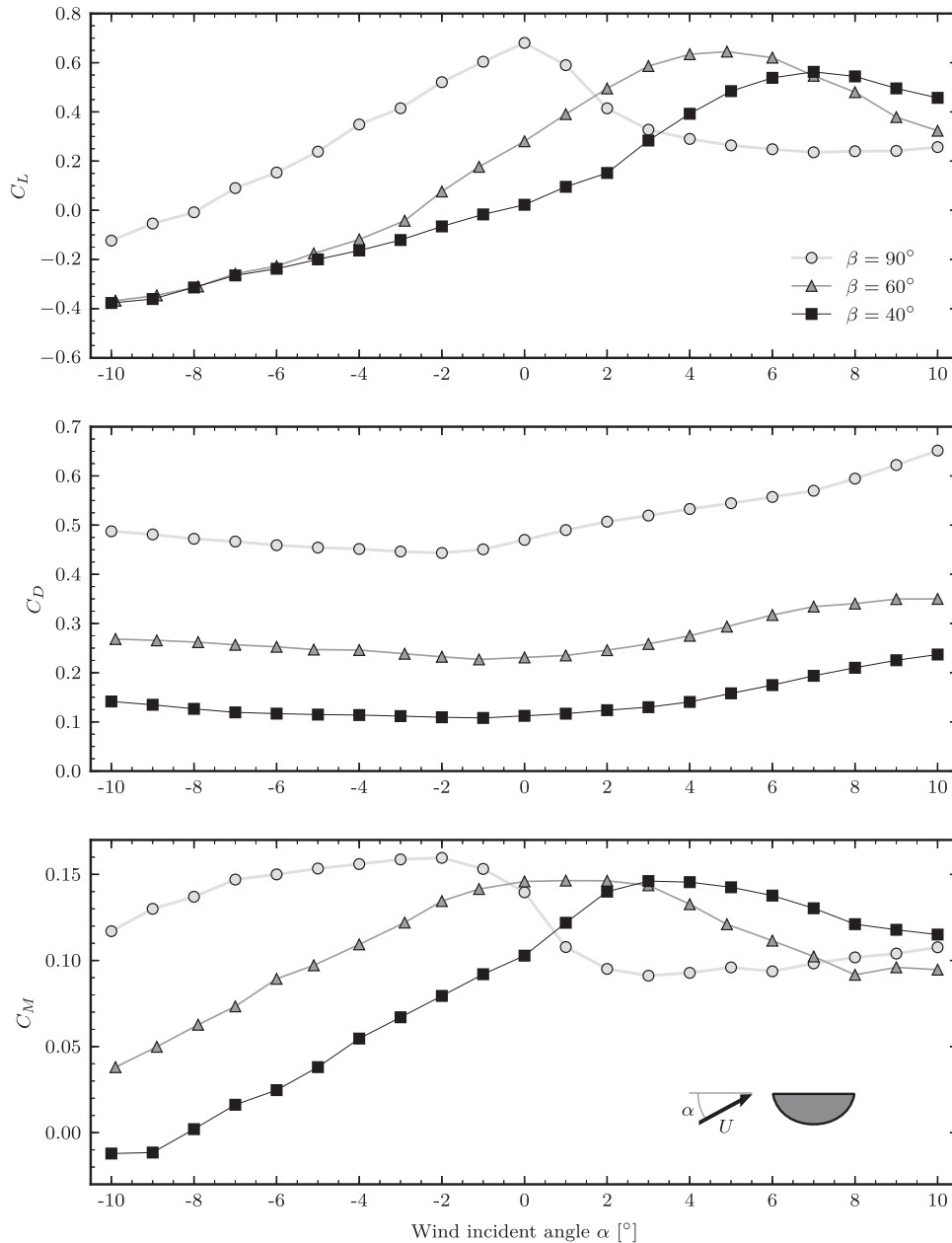


Figure 8. Force coefficients of models $\beta = 90^\circ$, $\beta = 60^\circ$ and $\beta = 40^\circ$ for a range of wind incident angle of $\alpha = [-10^\circ, 10^\circ]$.

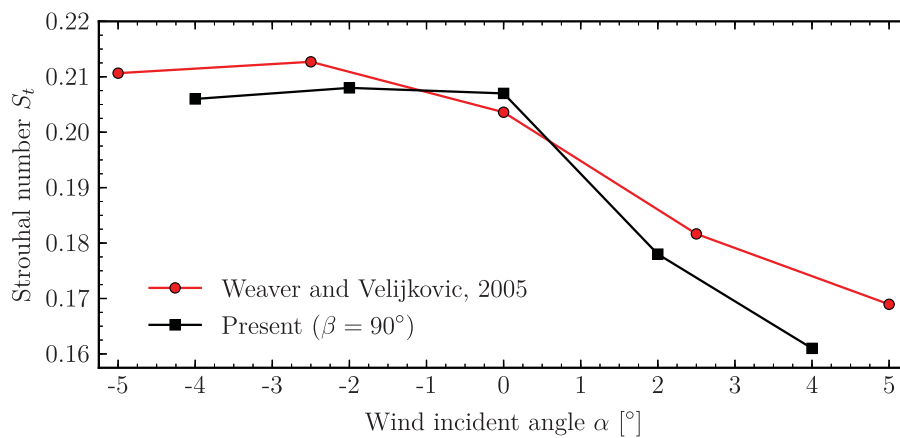
coefficient also shows a positive slope up to $\alpha = 4^\circ$. Conversely, the $\beta = 90^\circ$ case presents a non-streamlined behavior, easily identified by the lift coefficient curve and the negative slope in the moment coefficient. In addition, the drag coefficient presents high values, around 0.5. Similar curves can be found in Harris (1949) or Cheers (1950) for the C_D and in Novak and Tanaka (1974) for the C_M . The $\beta = 60^\circ$ case presents an intermediate behavior between $\beta = 40^\circ$ and $\beta = 90^\circ$. The C_L curve is similar to the $\beta = 40^\circ$ case, shifted backwards some degrees, showing the drop in the C_L in an intermediate point between $\beta = 90^\circ$ and $\beta = 40^\circ$ cases. The C_D reaches also an intermediate value between the other two curves, closer to the $\beta = 40^\circ$ geometry, as its sag is closer to

the one of that geometry. Finally, the C_M curve shows intermediate values between the other two.

In order to estimate the uncertainty associated to the experimental results used in this work to validate the CFD simulations, several tests have been conducted. They consist of defining the experimental values of the force coefficients at $\alpha = 0^\circ$ and $\alpha = 1^\circ$ as the mean value and standard deviation obtained from a sample of 25 tests carried out consecutively for each case. These values are reported in Table 2, where the 95% confidence intervals are also provided (Coleman & Steele, 2009). It must be noticed that the uncertainty estimated in this manner do not include all the possible sources of uncertainty (see Caracoglia, Sarkar, Haan, Sato, & Murakoshi, 2009;

Table 2. Mean value (μ), standard deviation (σ) and 95% confidence intervals for $n = 25$ samples ($\mu \pm 1.96 \cdot \sigma / \sqrt{n}$) of the experimental force coefficients of models $\beta = 40^\circ$, $\beta = 60^\circ$ and $\beta = 90^\circ$ at wind incident angle of $\alpha = 0^\circ$ and 1° .

Geometry	Parameter	$\alpha = 0^\circ$			$\alpha = 1^\circ$		
		C_L	C_D	C_M	C_L	C_D	C_M
$\beta = 90^\circ$	μ	0.681	0.470	0.140	0.591	0.492	0.108
	σ	0.010	0.005	0.008	0.022	0.005	0.005
	$\mu - 1.96 \cdot \sigma / \sqrt{n}$	0.677	0.468	0.136	0.583	0.490	0.106
	$\mu + 1.96 \cdot \sigma / \sqrt{n}$	0.685	0.472	0.143	0.599	0.494	0.110
$\beta = 60^\circ$	μ	0.275	0.231	0.146	0.391	0.235	0.146
	σ	0.012	0.005	0.008	0.011	0.005	0.007
	$\mu - 1.96 \cdot \sigma / \sqrt{n}$	0.271	0.230	0.143	0.386	0.233	0.144
	$\mu + 1.96 \cdot \sigma / \sqrt{n}$	0.280	0.233	0.149	0.395	0.237	0.149
$\beta = 40^\circ$	μ	0.022	0.112	0.103	0.095	0.117	0.122
	σ	0.008	0.003	0.006	0.008	0.004	0.007
	$\mu - 1.96 \cdot \sigma / \sqrt{n}$	0.019	0.111	0.100	0.092	0.115	0.119
	$\mu + 1.96 \cdot \sigma / \sqrt{n}$	0.026	0.114	0.105	0.098	0.118	0.125

**Figure 9.** Comparison of the Strouhal number as a function of the wind incident angle α for case $\beta = 90^\circ$ obtained by Weaver and Veljkovic (2005) and the results reported in this work.

Davenport, 1983; Kareem, 1988; Sarkar, Caracoglia, Haan, Sato, & Murakoshi, 2009), but provides a metric of deviation that helps to evaluate the agreement between the experimental and numerical results.

Furthermore, vortex shedding studies are carried out aiming to provide additional inputs for the validation of the CFD models which are discussed next. Besides, Weaver and Veljkovic (2005) reported the Strouhal numbers of their tests of the D-section, which is very useful as a reference for comparison with the experimental results presented in this work. Figure 9 compares the Strouhal number of the model $\beta = 90^\circ$ with those obtained for the same geometry in Weaver and Veljkovic (2005). It must be noticed that the characteristic dimension used in Weaver Veljkovic (2005) for the Strouhal number is the diameter of the geometry. Therefore, those results are reported divided by 2 in Figure 9, given that the characteristic dimension used in the present work for the Strouhal number is the sagitta (see Equation (1)). As it can be seen in Figure 9, there is a general agreement in the results, particularly for $\alpha = 0^\circ$. Moreover, a summary of the wind tunnel results of the Strouhal number obtained

Table 3. Strouhal number S_t of models $\beta = 40^\circ$, $\beta = 60^\circ$ and $\beta = 90^\circ$ for several wind incident angle values α .

Model	Wind incident angle α [°]				
	-4°	-2°	0°	2°	4°
$\beta = 90^\circ$	0.206	0.208	0.207	0.178	0.161
$\beta = 60^\circ$	0.215	0.210	0.198	0.185	0.172
$\beta = 40^\circ$	0.238	0.234	0.228	0.220	0.202

for the three models considering different angles of attack is presented in Table 3. The general trend is the decrease in the frequency of vortex shedding as the angle of attack increases. In the same manner, the lower the corner angle β is, the higher the frequency of the vortex shedding has been identified.

6. Numerical modeling, geometry and mesh description

6.1. Flow domain boundary conditions and numerical settings for OpenFOAM solver

The flow domain used in the CFD analyses is $40B$ wide and $30B$ high, being B the width of the cross-section. A

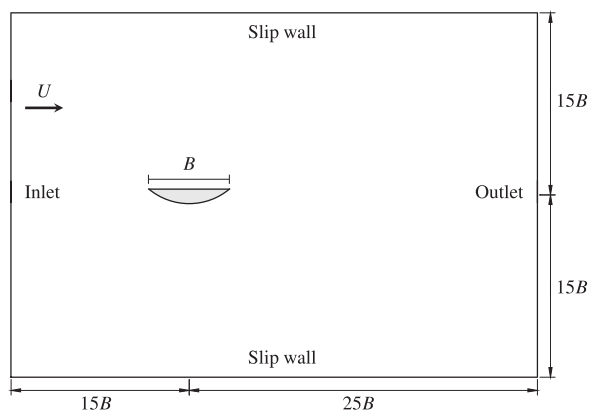


Figure 10. Definition of the flow domain and boundary conditions (not to scale).

conceptual sketch is presented in Figure 10, where the boundary conditions are also shown. At the left side of the flow domain is located the inlet, where Dirichlet conditions with a constant velocity of 4.4 m/s ($Re_B = 1 \cdot 10^5$) and low turbulence intensity characteristics are imposed. At the right side, a pressure outlet is placed with imposed atmospheric pressure. The lower and upper limits of the flow domain are considered slip walls.

The wall boundary condition on the surface of the studied body can be modeled by wall functions (Viegas & Rubesin, 1983) or by integration to the surface by means of a low Reynolds number wall modeling approach (Jones & Launder, 1972). In all the cases studied in this work the second approach was employed. The geometry of the cases under study follows the sketch of Figure 1, for the values of the corner angle $\beta = [40^\circ, 50^\circ, 60^\circ, 70^\circ, 80^\circ, 90^\circ]$. The corners of the cross-sections have been modeled as sharp.

An initial set of simulations were conducted using the $k - \omega$ SST turbulence model without corrections, using the OpenFOAM solver aiming to complete the verification studies that are reported next and obtaining a preliminary validation. The numerical schemes adopted in the simulations conducted in this investigation using the OpenFOAM CFD solver have been successfully applied in a previous published work by Nieto, Owen, et al. (2015). A summary is provided next. The PIMPLE algorithm has been used as transient solver. The interpolation of values from cell centers to face centers are conducted by a linear scheme. The gradient terms are discretized applying the Gauss scheme, adopting linear interpolation. For the divergence terms, the Gauss scheme is used, considering linear upwind and linear interpolation schemes. For the Laplacian terms, the Gaussian with a linear interpolation scheme and a limited normal surface gradient were employed. The first-order boundary implicit Euler scheme imposing a maximum Courant number of 1 was applied for the first

time derivative terms aiming to obtain a robust performance while keeping temporal diffusion at low levels (Guerrero, 2013). This approach has been successfully used in several research works, such as in Brusiani et al. (2013), Cid Montoya et al. (2018), Nieto, Hargreaves, et al. (2015), Nieto, Owen, et al. (2015), and Patruno (2015).

6.2. Verification of the finite volume grids

The design of the computational mesh plays an important role in the accuracy of the CFD results, and consequently it is a common practice to carry out verification studies. Verification aims to identify the grid for which the CFD model results are not sensitive to the chosen spatial discretization (see for instance, Manini, Soda, & Schewe, 2010). In this work, six meshes have been generated for the geometries considered in this study ($\beta = [40^\circ, 50^\circ, 60^\circ, 70^\circ, 80^\circ, 90^\circ]$), and three of them have been verified in order to assess the independence of the results with the spatial discretization, which correspond to the geometries analyzed experimentally ($\beta = [40^\circ, 60^\circ, 90^\circ]$). The verification studies were carried out adopting the Menter's SST $k - \omega$ turbulence model and the OpenFOAM solver.

Three different regions can be identified in all of the meshes considered in the verification study (see Figure 11). The first region (Region 1) consists of a block structured mesh made of hexahedral elements that cover roughly 90% of the flow domain, which is divided in a number of subdomains with higher element densities in critical regions, such as the wake of the circular segment or the vicinity of the body. Another region is the boundary layer mesh (Region 2), that presents the highest mesh density since a low Reynolds wall modeling approach is adopted. In this region a structured mesh is adopted. The third region is the so-called buffer region mesh (Region 3), which covers the area close to the circular cylinder, linking the block structured mesh and the boundary layer mesh. This is an unstructured mesh, where triangular prisms have been adopted.

The refinement strategy adopted to carry out the verification studies was conducted as follows. In the general block structured mesh region (Region 1), the number of elements along the edges has been systematically increased by a factor of 100/82 and 122/100 which is roughly 1.22. The scale distribution is kept constant for the three meshes in the grid-refinement study. In the boundary layer mesh region (Region 2) the number of elements around the section was systematically changed according to the following factors: 660/540 and 804/660 along the rectilinear side of the section, and 1060/864 and 1292/1060 along the curvilinear side, which gives also a

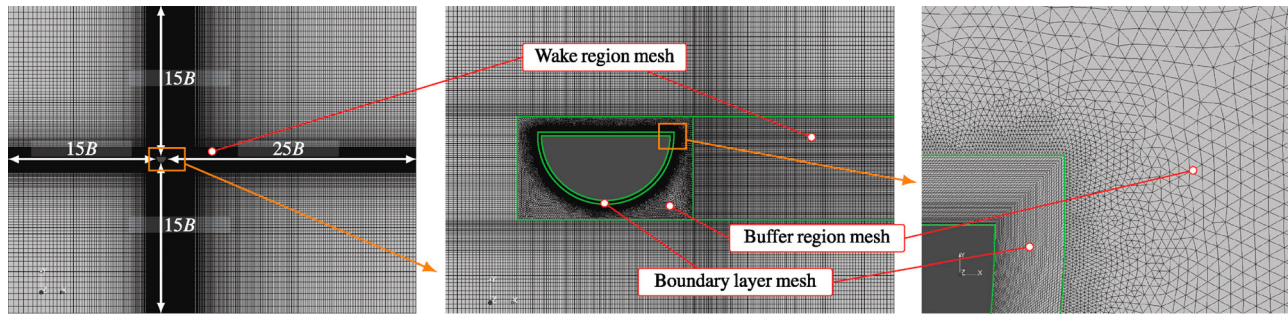


Figure 11. Mesh used for section $\beta = 90^\circ$.

growth ratio of about 1.22, as in Region 1. The width to depth ratios of the elements in the first row attached to the body vary between 5.463 and 3.67 depending on the mesh density and the rectilinear or curved side of the section. The height of the boundary layer mesh, the number of rows and the growth ratio has been kept constant (Roache, 2009) because in this manner it could be guaranteed that the limitations concerning mean and maximum allowable values of y^+ were uniformly satisfied for the three cases studied. In the buffer mesh region (Region 3) no systematic refinement was conducted due to the user-interaction-based definition of this mesh, and the need to produce smooth transitions between elements in Region 1 and Region 2.

The refinement approach adopted is not a systematic strategy given the co-existence of structured and unstructured grid regions and the required user intervention for the refinement in the unstructured buffer region. This kind of meshes and refinement approaches are commonly used in civil engineering applications (see for instance Cid Montoya et al., 2018; Mannini, Šoda, Voß, & Schewe, 2010; Nieto et al., 2015) where standard

methods of grid-convergence studies are difficult to apply rigorously (Mannini et al., 2010), and may require grid densities higher than those typical of practical computations (Pelletier, 2008; Salas & Atkins, 2009). Consequently, the Grid Convergence Index (Roache, 2009) was not used for the verifications studies reported in this work.

The result of the study for $\beta = 90^\circ$ geometry considering an angle of attack $\alpha = 0^\circ$ is shown in Table 4. In this table, the total number of cells and the number of cells in the boundary layer (BL) mesh around the deck section are indicated, as well as the values of the effective grid refinement index Effective r (Roache, 2009), defined as

$$\text{Effective } r = \left(\frac{N_1}{N_2} \right)^{1/D}, \quad (35)$$

where N_1 and N_2 are the number of elements in the fine and coarse meshes, and D is the dimensionality of the problem. The force coefficients and Strouhal number provided in this table and in the following sections of this work are obtained considering an averaging cycle

Table 4. Properties and results of the grid-refinement study for the D-section ($\beta = 90^\circ$).

Grid	BL cells	Total cells	Effective r	S_r	C_L	C_D	C_M	C_L'	C_D'	C_M'
Coarse	70200	199689	–	0.217	0.676	0.440	0.153	0.314	0.041	0.049
Medium	86000	270098	1.16	0.211	0.672	0.437	0.153	0.314	0.041	0.049
Fine	104800	362789	1.16	0.210	0.677	0.442	0.155	0.321	0.041	0.050
Experimental				0.207	0.681	0.470	0.140	–	–	–

Table 5. Properties of the meshes for each geometry, where Reg. 1 is the boundary layer (BL) mesh, Reg. 2 is the buffer region mesh, Reg. 3 is the wake region mesh, p means number of elements in the perimeter, δ_1 is the height of the first element, h is the height of the boundary layer mesh, No. is the number of rows in the BL mesh, \hat{r} the growing ratio, AR_r the first row aspect ratio over the rectilinear side and AR_c the first row aspect ratio over the curved side.

$\beta [^\circ]$	Number of cells				Boundary layer definition							y^+		
	Total	Reg. 1	Reg. 2	Reg. 3	p	δ_1/B	h/B	No.	\hat{r}	AR_r	AR_c	Mean	Max	$y^+ > 4$ [%]
40	321,050	135,000	113,680	72,370	1960	3.24×10^{-4}	3.82×10^{-2}	58	1.023	3.435	3.167	1.498	6.037	0.102
50	318,809	135,000	113,680	70,129	1960	3.24×10^{-4}	3.82×10^{-2}	58	1.023	3.434	3.322	1.451	6.220	0.102
60	296,846	135,000	99,760	62,086	1720	3.24×10^{-4}	3.82×10^{-2}	58	1.023	4.683	3.526	1.256	6.446	0.174
70	314,927	135,000	113,680	66,247	1960	3.24×10^{-4}	3.82×10^{-2}	58	1.023	3.435	3.791	1.242	6.472	0.204
80	272,288	135,000	86,000	51,288	1720	3.39×10^{-4}	3.82×10^{-2}	50	1.030	4.479	3.955	1.306	5.932	0.174
90	270,098	135,000	86,000	49,098	1720	3.39×10^{-4}	3.82×10^{-2}	50	1.030	4.482	4.383	1.350	6.384	0.291

of a minimum of 25 non-dimensional time units after the results can be considered periodic.

Small discrepancies in the three verification studies have been found between the coarse and medium meshes. Differences between medium and fine meshes are mostly negligible. Consequently, the medium meshes have been adopted hereafter for further analyses. The characteristics of the six meshes adopted in this study are reported in Table 5, where the mesh properties of the geometries $\beta = 50^\circ$, 70° and 80° are established based on the results of the verification studies previously reported. These meshes are the ones adopted for all the CFD simulations that are discussed in Section 7. The number of cells in each region of the mesh is provided in Table 5, presenting an average total number of cells of $3 \cdot 10^5$. These regions can be identified in Figure 11, where the mesh used for the case $\beta = 90^\circ$ is shown. Moreover, Table 5 describes the boundary layer mesh defined for each geometry and the dimensionless wall distances $y^+ = (\delta_1 u_*)/v$, where u_* is the friction velocity and δ_1 is the height of the first element. These dimensionless wall distances present mean values lower than 1.5, and the maximum values are below 6.5 for the considered Reynolds number ($Re_B = 1 \cdot 10^5$). A maximum Courant number of $Co = 1$ was imposed, which leads to mean non-dimensional time step values in the range $\bar{\Delta}t = \bar{\Delta}t U/B \approx 2.2 \cdot 10^{-4}$, depending on the particular simulation being considered.

6.3. Turbulence modeling alternatives

The results obtained from the CFD simulations conducted with the OpenFOAM solver and the $k - \omega$ SST turbulence model during the verification studies were unable to match the wind tunnel results at $\alpha = 0^\circ$ for $\beta = 60^\circ$ and $\beta = 40^\circ$ geometries. It has already been commented upon in Section 2, that the ability of a CFD

model to properly simulate the aerodynamic responses of interest is dependent on the ability of the turbulence models to properly emulate the complex phenomena that take place, such as turbulent transition or the effects of streamline curvature. Therefore, alternative turbulence models, or corrected versions of the $k - \omega$ SST, have been considered: $k - \omega$ SST with low-Reynolds-number correction (LRNC), $k - \omega$ SST with low-Reynolds-number and curvature corrections (LNRC & CC), and four-equation Transition SST models.

The simulations where the LRNC, LNRC & CC and Transition SST turbulence models are applied have been conducted using the commercial ANSYS Fluent solver (Ansys fluent theory guide, 2013).

6.4. Assessment of the impact of different solvers, mesh typology and numerical settings for the ANSYS solver

When an aerodynamics problem is studied by means of a numerical simulation, different modeling and setup alternatives are available. Consequently, certain dispersion in the numerical predictions of different quantities must be expected (Bruno et al., 2014). This means that a certain problem can be addressed adopting different numerical setups, different spatial and temporal discretizations and different modeling approaches obtaining, for well posed

Table 6. Comparison of the results for the case $\beta = 90^\circ$ using the $k - \omega$ SST turbulence model with the open source solver OpenFOAM using the settings described in Section 6.1 and the ANSYS Fluent solver with the settings described in Section 6.4.

Solver	Mesh	C_L	C_D	C_M	S_f
OpenFOAM	M1	0.672	0.437	0.152	0.211
OpenFOAM	M2	0.716	0.443	0.157	0.211
ANSYS Fluent	M2	0.636	0.421	0.153	0.217

Note: Two different meshes are also used, which are described in Sections 6.2 and 6.4.

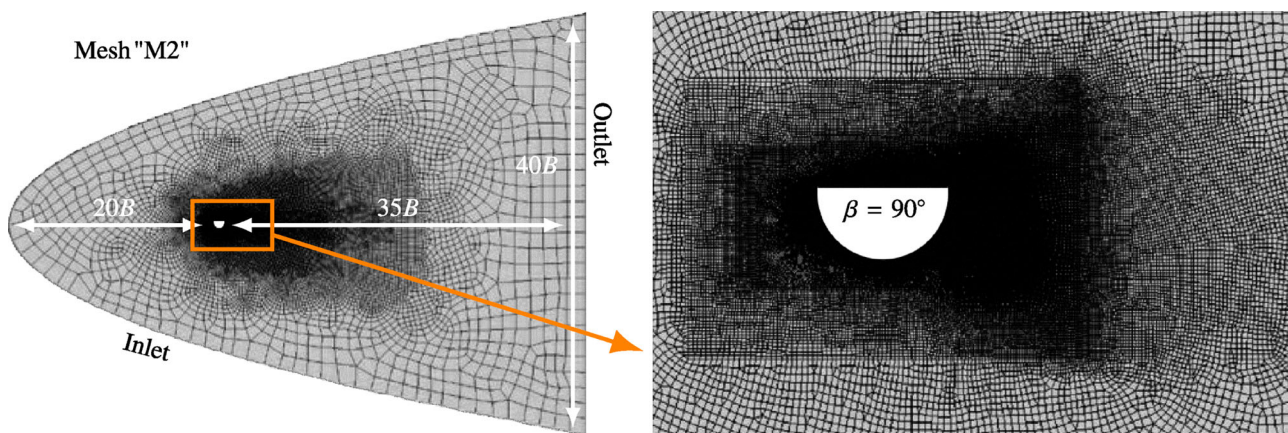


Figure 12. Details of the non-structured quadrangular mesh with parabolic flow domain shape identified as 'M2' in Table 6.

models, correct results within the limits of the logical dispersion in the quantities of interest. With the purpose of making clear that the dramatic differences in the results that are reported in Section 7 are due to the different turbulence models adopted, and not the solver, the numerical settings or the spatial and temporal discretizations, for the same reference case ($\beta = 90^\circ$ at $\alpha = 0^\circ$) three different numerical simulations have been set up and the results are reported in Table 6. The first simulation corresponds to the medium mesh case reported in Section 6.2, (mesh 'M1' in Table 6) where the turbulence model is the standard version of Menter's $k - \omega$ SST and the solver of choice has been OpenFOAM. In the second simulation, the same solver, turbulence model and numerical settings as in the former one are adopted; however a 420,000 cells non-structured quadrangular mesh identified as 'M2', with a parabolic flow domain shape, as shown in Figure 12, is adopted ($\delta_1/B = 1.66 \cdot 10^{-4}$), aiming to assess the effect caused by a different spatial discretization. Finally, in the third simulation, the non-structured quadrangular mesh (M2) is chosen along with the ANSYS solver. For the CFD simulations conducted with ANSYS the numerical settings adopted are based on the previous experience of the authors with this CFD solver (Nieto, Hernández, Jurado, & Baldomir, 2010; Nieto, Kusano, Hernández, & Jurado, 2010). The pressure-velocity coupling is carried out adopting the PISO scheme with neighbor and skewness corrections. The interpolation values from cell centers are based upon the Green-Gauss gradient scheme. The discretization for the momentum, turbulence kinetic energy and turbulence dissipation rate are conducted adopting second-order interpolation schemes. The solver considers second-order unsteady formulation. The non-dimensional time step is $\Delta s = \Delta t U/B = 1.5 \cdot 10^{-3}$ (Nieto, Hernández, Kusano, & Jurado, 2012), and the Standard version of the $k - \omega$ SST turbulence model is adopted. The similitude in the results obtained for the force coefficients and Strouhal number when the turbulence model is the same in the three numerical simulations, signals the adequacy of the numerical settings, solvers, and spatial and temporal discretizations adopted in the simulations whose results are discussed in the next section. In Table 6 only the

lift coefficient shows small differences depending on the CFD model considered. Consequently, the discrepancies in the results that are reported in the following section, can be attributed solely to the different turbulence models considered, and may therefore be used as the basis for the assessment of the reliability of the considered turbulence models in this particular problem.

7. Results and discussion

The numerical results obtained for the six geometries of circular segments under study at 0° and 1° angles of attack are reported in the following subsections. The meshes described in Section 6.2 and Table 5 are the ones adopted for each geometry in all the simulations reported in this section. The CFD-based results are validated with the available experimental data previously reported in Section 5. As a first approach, all the considered geometries of circular segments have been analyzed by means of the standard version of Menter's $k - \omega$ SST turbulence model using the OpenFOAM solver and the settings reported in Section 6.1. The limitations of this approach to properly simulate the complex aerodynamic phenomena that take place in some geometries and angles of attack are evident when the numerical results are compared with the wind tunnel data. Therefore, corrections in the $k - \omega$ SST turbulence model or other turbulence models capable of accurately simulate transition must be adopted for improving the predictive capabilities of the CFD models. For these simulations adopting the LRNC, LRNC&CC and Transition SST turbulence models, the solver of choice has been ANSYS, and the numerical settings adopted are the ones described in Section 6.4.

7.1. $\beta = 90^\circ$ case

The $\beta = 90^\circ$ geometry ($B/H = 2$, $Re_R = 0.5 \cdot 10^5$) has been the first case to be analyzed by means of the $k - \omega$ SST turbulence model. Hence, a first step in the validation process is to compare the experimental results reported in Section 5.4 with the numerical ones obtained using the $k - \omega$ SST model for angles of attack $\alpha = 0^\circ$ and 1° . Table 7 presents a comparison between these results and

Table 7. Summary of the force coefficients obtained experimentally (Exp) and numerically by means of the $k - \omega$ SST turbulence model ($k - \omega$ SST) and their relative ($\delta_{k-\omega\text{SST}}$) and absolute ($\Delta_{k-\omega\text{SST}}$) errors for the geometry $\beta = 90^\circ$ considering angles of attack $\alpha = 0^\circ$ and 1° .

Case	$\beta = 90^\circ (\alpha = 0^\circ)$				$\beta = 90^\circ (\alpha = 1^\circ)$			
	C_L	C_D	C_M	S_f	C_L	C_D	C_M	S_f
Exp	0.681	0.470	0.140	0.207	0.591	0.492	0.108	0.205
$k - \omega$ SST	0.672	0.437	0.152	0.211	0.648	0.450	0.129	0.206
$\delta_{k-\omega\text{SST}}$ [%]	1.322	7.021	8.571	1.932	9.645	8.537	19.444	0.370
$\Delta_{k-\omega\text{SST}}$	0.009	0.033	0.012	0.004	0.057	0.042	0.021	0.001

also the relative (δ) and absolute (Δ) errors between the experimental and numerical data.

The $\beta = 90^\circ$ geometry, for both angles of attack ($\alpha = [0^\circ, 1^\circ]$), presents low values of absolute errors, and a maximum relative error of 19.4% for the C_M at $\alpha = 0^\circ$, which must not be overemphasized, since it corresponds to an absolute error in the moment coefficient value of 0.02. The C_L , C_D and S_t values show reduced relative and absolute errors. In general, it can be assumed that the results present fair agreement for this geometry.

Figure 13 shows the instantaneous flow velocity U and turbulence kinetic energy k fields obtained for this case at both angles of attack, using the $k - \omega$ SST turbulence model. In the representation of the flow velocity field, the streamlines are shown to help identifying the flow fundamental features. The instantaneous fields correspond to a maximum lift coefficient instant in the time history. It can be seen that the separation point over the curved side is close to 90° (considering anti-clockwise direction and 0° at the windward corner of the cross-section). This is similar to the classical flow structure in the sub-critical regime, as described in Schewe (2001), Zdravkovich (1997), Achenbach and Heinecke (1981) and Kwok (1986) for circular cylinders. It must be noticed that, taking the results of the Reynolds-number sensitivity studies into account, reported in Figure 7, this is the expected flow structure for this section. This coincidence shows the ability of the $k - \omega$ SST turbulence model to reproduce the experimental results for this geometry, as reported in Table 7. In the rectilinear side, the separation point is located at the windward corner, generating a bubble of roughly the same length as the width of the section. The flow structure on the rectilinear side can be qualitatively compared to the flow structure of the rectangular 2:1 cylinder (since this is the B/H ratio of the $\beta = 90^\circ$ section), which shows a separated-type behavior, as described in Shimada and Ishihara (2002). Although the flow structures for both angles of attack are similar, it can be appreciated that the bubble at $\alpha = 1^\circ$ is larger than at $\alpha = 0^\circ$.

The turbulence kinetic energy instantaneous fields show the growth in the turbulent energy along the shear layer on the rectilinear side, reaching the maximum value close to the leeward corner. On the other hand, the turbulent energy in the shear layer detached from the curved side grows smoothly, reaching a maximum value about half of the one in the upper shear layer. Besides, these flow fields allow to visualize the interaction between the two shear layers in the wake of the D-section.

7.2. $\beta = 40^\circ$ case

In this section, the CFD-based simulations of the geometry showing the lowest value in the corner angle and

chord to sagitta ratio are studied. Due to the low B/H ratio, a permanently reattached shear layer is expected on the rectilinear surface, which is completely different from the aerodynamic behavior of the $\beta = 90^\circ$ geometry. The results of the $\beta = 40^\circ$ case ($B/H = 5.5$, $Re_R = 0.778 \cdot 10^5$) at 0° angle of attack obtained using the $k - \omega$ SST turbulence model present unacceptable absolute and relative errors for all the force coefficients and Strouhal numbers when they are compared with wind tunnel tests. In fact, the strong decrement in the lift coefficient obtained in the CFD simulations (see Table 8), in combination with the also low value in the drag coefficient, are indicative of this circular segment showing a super-critical regime behavior at a too low Reynolds number. This is typical of two-equation turbulence models in the absence of Low-Reynolds corrections. Consequently, further numerical analyses of this geometry should be conducted adopting alternative formulations for the turbulence model.

A first approach for improving the predictive capabilities of the CFD model has been to adopt low-Reynolds-number corrections (LRNC) in the $k - \omega$ SST turbulence model, given its ability to grossly simulate transition (Wilcox, 1993). It can be seen in Table 8 that when the low-Reynolds-number corrections are introduced in the $k - \omega$ SST turbulence model, the improvements are remarkable, since all the coefficients present now acceptable similitude when they are compared with the experimental results. The main improvement has been obtained in the C_L , where the absolute error has been decreased from 0.361 to 0.087. Relevant improvements have also been obtained for the C_D and the S_t , and the accuracy in the C_M value is similar.

These improvements in the force coefficients and Strouhal number are caused by a better prediction of transition, which avoids the anticipation of the Reynolds-number effect that switches the flow regime from sub-critical to super-critical, as it can be appreciated from the values of the averaged force coefficients (see Section 5.3). This can be analyzed by studying the flow structures simulated by the $k - \omega$ SST turbulence model with and

Table 8. Comparison of the results for the case $\beta = 40^\circ$ for an angle of attack $\alpha = 0^\circ$ using the $k - \omega$ SST turbulence model with and without low-Reynolds-number correction (LRNC).

Case	$\beta = 40^\circ (\alpha = 0^\circ)$			
	C_L	C_D	C_M	S_t
Exp	0.022	0.112	0.103	0.228
$k - \omega$ SST	-0.322	0.056	0.064	0.310
$\delta_{k-\omega}$ [%]	1563.636	50.000	37.864	35.965
$\Delta_{k-\omega}$	0.344	0.056	0.039	0.082
LRNC	-0.049	0.105	0.116	0.243
δ_{LRNC} [%]	322.727	6.250	12.621	6.579
Δ_{LRNC}	0.071	0.007	0.013	0.015

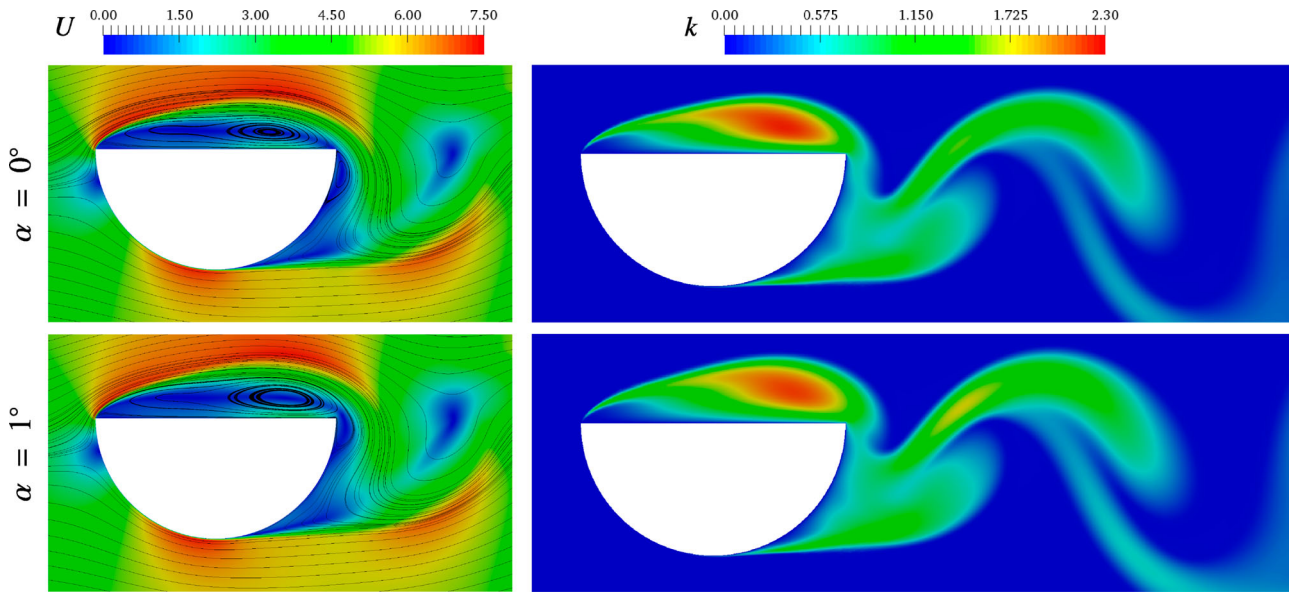


Figure 13. Flow velocity U and turbulence kinetic energy k fields obtained for $\beta = 90^\circ$ with angles of attack $\alpha = 0^\circ$ and $\alpha = 1^\circ$ using the $k - \omega$ SST turbulence model. The instantaneous fields correspond to the maximum lift in the periodic time history ($\theta = \pi/2$).

without low-Reynolds-number corrections, which are reported in Figures 14 and 15.

In Figure 14, the instantaneous velocity field obtained applying the $k - \omega$ SST model with and without low-Reynolds-number corrections are compared at an instant in the time-history close to the maximum in the lift coefficient during one cycle of the lift coefficient time history ($\theta = \pi/2$). In this figure, it can be appreciated how the $k - \omega$ SST turbulence model without corrections anticipates the change of flow regime to super-critical (high Re), as it has been described in

Schewe (1986). In the curved side, the separation point is located further downstream because the boundary layer undergoes transition and the fluid closest to the surface has increased its momentum. Over the rectilinear side, the reattachment point is located about $0.25B$, consistently with the response of the flow in the rectilinear side of the cross-section of the Great Belt approach span deck reported by Schewe (2001) for the super-critical regime. The permanent reattachment on the rectilinear side is consistent with the flow structure reported for rectangular cylinders with aspect ratio

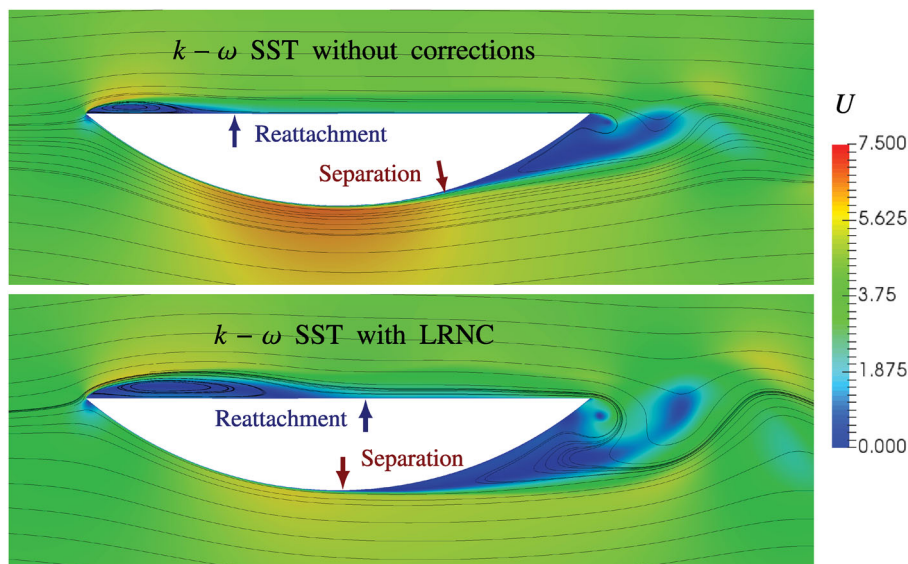


Figure 14. Flow velocity U field obtained for $\beta = 40^\circ$ at $\alpha = 0^\circ$ using the $k - \omega$ SST turbulence model without corrections and with low-Reynolds-number corrections. The instantaneous fields correspond to the maximum lift in the periodic time history ($\theta = \pi/2$). The reattachment point in the straight side and the separation point in the curved side are indicated for comparative purposes.

similar to this geometry $B/H = 5.5$, as reported in Shimada and Ishihara (2002) and Bruno et al. (2014) among others.

On the other hand, when the low-Reynolds-number corrections are introduced in the $k - \omega$ SST turbulence model, the flow structure corresponds to what is expected inside the sub-critical region. It can be seen in Figure 14 how the separation point in the curved side has moved upstream in the simulation using the $k - \omega$ SST turbulence model with low-Reynolds-number corrections, as described in Wilcox (2011) for circular cylinders, which has a dramatic effect on the lift coefficient (see Figure 7). Similar flow patterns for circular cylinders can be found in Van Dyke (1982). In this simulation, the reattachment point on the rectilinear side is located farther than $0.5B$ from the windward corner. Similar response is found by Schewe (2001) for the sub-critical regime of the Great Belt approach span cross-section.

As a consequence of the different location of the separation and reattachment points and turbulent energy content in shear layers and boundary layers, differences in the wakes of both simulations can be found. This can be noticed in Figure 15 by comparing the instantaneous turbulence kinetic energy k fields at the maximum lift instant during one cycle of the lift time history ($\theta = \pi/2$). In the $k - \omega$ SST simulation without corrections, the wake is narrower than when the low-Reynolds-number correction is included, which is typical of the response at high Re (Schewe, 2001). This phenomenon is also described in Schewe (1986) and in Wilcox (2011) for circular cylinders. In addition, it can be appreciated from the wake structure reported in Figure 15 that the S_t grows in the super-critical regime (see also Table 8 and refer to Figure 7), as it has also been reported by Schewe

and Larsen (1998) for several bluff bodies. Similar comparisons can be made for the C_D , that decreases inside the super-critical region.

Hence, the low-Reynolds-number correction applied to the $k - \omega$ SST turbulence model has successfully avoided the anticipation of transition in the boundary layer and in the shear layer, responsible for the changes in the flow regime from sub-critical to super-critical, as described in Section 5.3. Similar performance of this correction has been reported in the work by Collie et al. (2008) for flat plates at small angles of attack.

However, the aerodynamic behavior of the $\beta = 40^\circ$ case when the incident angle is $\alpha = 1^\circ$ is still inadequate even though low-Reynolds-number corrections are included in the $k - \omega$ SST turbulence model, as shown in Table 9. This points towards the coincidental ability of the corrected versions of the $k - \omega$ SST turbulence model to simulate transition (Menter et al., 2006) as it had been remarked in the Introduction of this work (Section 1). Hence, further corrections in the turbulence model have been considered.

The inclusion of the Spalart–Shur correction when modeling body geometries with curved shapes has shown good results in several published works. For instance, it was found in Ahmad et al. (2013) that this correction helps to obtain better predictions in the wake region of the flow around an airfoil. Therefore, the Spalart–Shur correction is adopted in the $k - \omega$ SST turbulence model, together with the low-Reynolds-number correction, aiming to improve the numerical results for the $\beta = 40^\circ$ case when the angle of attack is $\alpha = 1^\circ$. The results are reported in Table 9, where the force coefficients and Strouhal numbers obtained by the $k - \omega$ SST turbulence model without corrections are compared with the

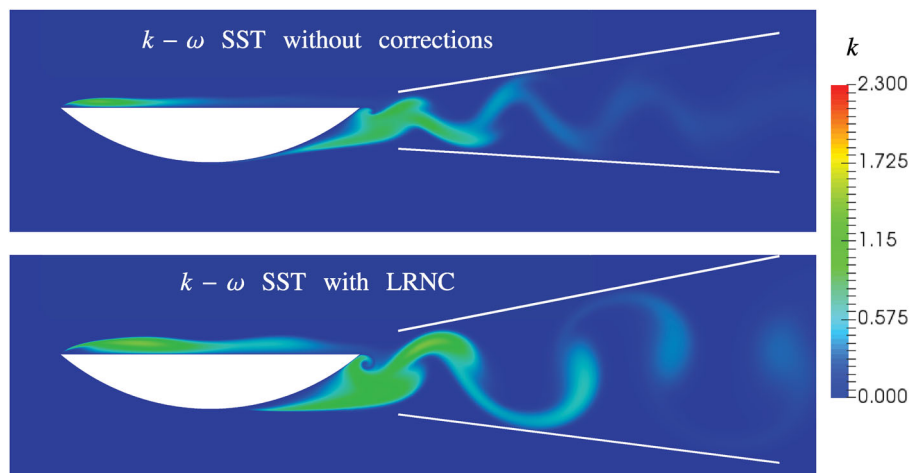


Figure 15. Turbulence kinetic energy k field obtained for $\beta = 40^\circ$ at $\alpha = 0^\circ$ using the $k - \omega$ SST turbulence model without corrections and with low-Reynolds-number corrections. The instantaneous fields correspond to the maximum lift in the periodic time history ($\theta = \pi/2$).

Table 9. Comparison of the results for the case $\beta = 40^\circ$ for an angle of attack $\alpha = 1^\circ$ using the $k - \omega$ SST turbulence model with and without low-Reynolds-number correction (LRNC) and curvature correction (CC).

Case	C_L	C_D	C_M	S_t
Exp	0.095	0.117	0.122	0.219
$k - \omega$ SST	-0.151	0.063	0.094	0.281
$\delta_{k-\omega}$ [%]	258.947	46.154	22.951	28.311
$\Delta_{k-\omega}$	0.246	0.054	0.028	0.062
LRNC*	0.350*	0.100*	0.135*	0.229*
δ_{LRNC} [%]	268.421	14.530	10.656	4.566
Δ_{LRNC}	0.255	0.017	0.013	0.010
LRNC & CC	0.048	0.112	0.134	0.238
$\delta_{LRNC \& CC}$ [%]	49.474	4.274	9.836	8.676
$\Delta_{LRNC \& CC}$	0.047	0.005	0.012	0.019

*Results at a non dimensional time of $\bar{t} = tU/B = 143$ once it was clear the tendency of the simulation towards incorrect values and stationary response.

results achieved when both corrections are considered. It can be seen that the simulation including simultaneously the curvature and low-Reynolds-number corrections in the $k - \omega$ SST turbulence model provides results in agreement with the experimental ones. The lower value obtained for the lift coefficient is consistent with

Table 10. Comparison of the results for the case $\beta = 60^\circ$ for an angle of attack $\alpha = 0^\circ$ using the $k - \omega$ SST turbulence model with and without low-Reynolds-number correction (LRNC).

Case	$\beta = 60^\circ (\alpha = 0^\circ)$			
	C_L	C_D	C_M	S_t
Exp	0.275	0.231	0.146	0.198
$k - \omega$ SST	0.287	0.137	0.126	0.022
$\delta_{k-\omega}$ [%]	4.364	40.693	13.699	88.889
$\Delta_{k-\omega}$	0.012	0.094	0.020	0.176
LRNC	0.280	0.247	0.169	0.210
δ_{LRNC} [%]	1.818	6.926	15.753	6.061
Δ_{LRNC}	0.005	0.016	0.023	0.012

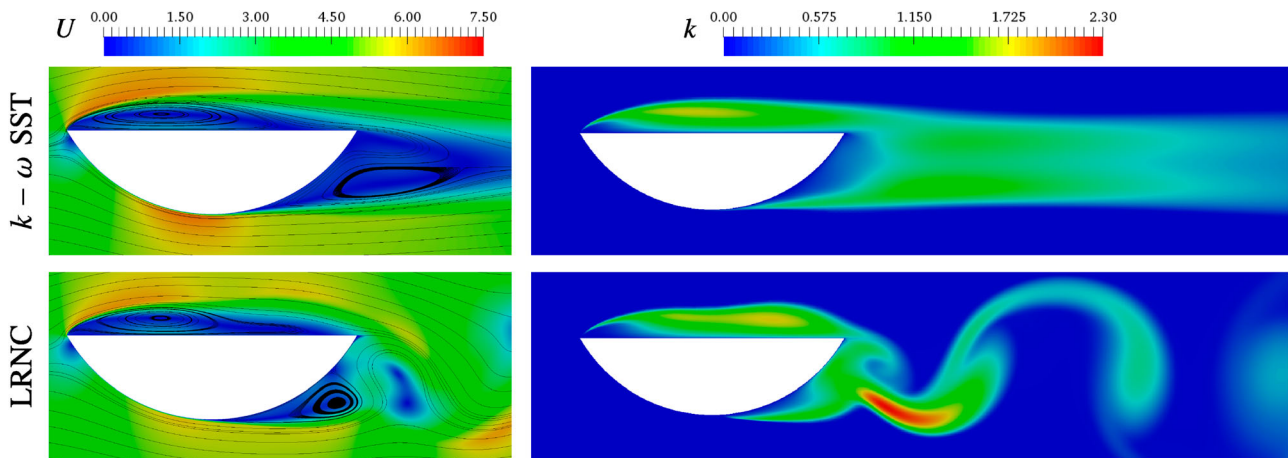


Figure 16. Flow velocity U and turbulence kinetic energy k fields obtained for $\beta = 60^\circ$ at $\alpha = 0^\circ$ using the $k - \omega$ SST turbulence model without and with low-Reynolds-number corrections. The instantaneous fields correspond to the maximum lift in the periodic time history ($\theta = \pi/2$).

the numerical result obtained for $\alpha = 0^\circ$ using the $k - \omega$ SST turbulence model with the low-Reynolds-number correction (see Table 8). The flow fields and their interpretation for the $\beta = 40^\circ$ case at $\alpha = 1^\circ$ are substantially similar to those obtained for $\alpha = 0^\circ$ that were shown in Figures 14 and 15.

7.3. $\beta = 60^\circ$ case

This corner angle ($B/H = 3.46$, $Re_R = 0.577 \cdot 10^5$) represents the intermediate case in the geometries that have been experimentally tested. In this case, some of the values of the force coefficients obtained with the $k - \omega$ SST turbulence model present non-negligible discrepancies with the experimental data (see Table 10). This is the case of the Strouhal number, where the wind tunnel test value is about 0.20, and the numerical simulation at $\alpha = 0^\circ$ produces almost stationary results ($S_t = 0.022$). In addition, although the results for the C_L and C_M can be considered acceptable, C_D values present also noticeable discrepancies.

The aerodynamic response of the $\beta = 60^\circ$ section at $\alpha = 0^\circ$ is in general very much improved by using the low-Reynolds-number corrected version of the $k - \omega$ SST turbulence model. The improvement in the C_D is noticeable, increasing its value and therefore reducing the absolute error from 0.082 to 0.028. Furthermore, the flow is not stationary, reporting a value of Strouhal number of $S_t = 0.21$. The absolute error in the C_M is again small, $\Delta_{C_M} = 0.046$.

The differences in the flow structure provided by both simulations can be appreciated in Figure 16 where the instantaneous flow fields are provided for $\theta = \pi/2$ during one cycle of the lift time history. As it can be anticipated from the value of the Strouhal number reported in Table 10, the $k - \omega$ SST turbulence model

Table 11. Comparison of the results for the case $\beta = 60^\circ$ for an angle of attack $\alpha = 1^\circ$ using the $k - \omega$ SST turbulence model with and without low-Reynolds-number correction (LRNC) and curvature correction (CC).

Case	C_L	C_D	C_M	S_t
Exp	0.391	0.235	0.146	0.191
$k - \omega$ SST	0.319	0.150	0.117	0.024
$\delta_{k-\omega}$ [%]	18.414	36.170	19.863	87.244
$\Delta_{k-\omega}$	0.072	0.085	0.029	0.166
LRNC	0.572	0.220	0.148	0.190
δ_{LRNC} [%]	46.292	6.383	1.370	0.524
Δ_{LRNC}	0.181	0.015	0.002	0.001
LRNC & CC	0.517	0.274	0.157	0.201
$\delta_{LRNC \& LRNC}$ [%]	32.225	16.596	7.534	5.236
$\Delta_{LRNC \& LRNC}$	0.126	0.039	0.011	0.010

provides a stationary response, which differs from the non-stationary results obtained experimentally. When the low-Reynolds-number corrections are introduced, the simulation produces a flow structure characteristic of the sub-critical regime, as described in Section 7.2. This general improvement when LRNC are introduced to the $k - \omega$ SST turbulence model at $\alpha = 0^\circ$ is consistent with the data previously reported for $\beta = 40^\circ$.

When the angle of attack is $\alpha = 1^\circ$, the standard version of Menter's $k - \omega$ SST turbulence model also produces an almost stationary response, and non-negligible differences in the force coefficients are apparent. Introducing the low-Reynolds-number corrections is insufficient to properly simulate the aerodynamic response of the section. This is also reflected in the lift coefficient, which presents a relative error of $\Delta_{C_L} = 40.5\%$ when compared with the experimental value as shown in Table 11.

As it happened with the $\beta = 40^\circ$ case at $\alpha = 1^\circ$, the inclusion of the curvature correction in the turbulence

Table 12. Results obtained for geometries $\beta = 80^\circ$ and $\beta = 70^\circ$ at $\alpha = 0^\circ$ and $\alpha = 1^\circ$ using the $k - \omega$ SST turbulence model.

Section	Method	Angle α	C_L	C_D	C_M	S_t
$\beta = 80^\circ$	$k - \omega$ SST	0°	0.406	0.294	0.145	0.206
		1°	0.489	0.353	0.160	0.201
$\beta = 70^\circ$	$k - \omega$ SST	0°	0.368	0.201	0.130	0.180
		1°	0.363	0.222	0.124	0.182

model gives place to a more reliable modelization of the phenomenon, providing a set of force coefficients closer to the experimental results. Furthermore, it can be seen in Figure 17 ($\theta = \pi/2$) that the structure of the flow corresponds to the sub-critical regime with characteristics similar to the ones described for $\beta = 90^\circ$ and $\beta = 40^\circ$ cases.

7.4. $\beta = 80^\circ$ and $\beta = 70^\circ$ cases

For the sections for which experimental data were not available to validate the numerical results, the selection of the most adequate turbulence model has been made based on the performance of the turbulence models in the closest geometries that had been tested in the wind tunnel. Hence, geometries $\beta = 80^\circ$ ($B/H = 2.38$, $Re_R = 0.508 \cdot 10^5$) and $\beta = 70^\circ$ ($B/H = 2.85$, $Re_R = 0.532 \cdot 10^5$) are numerically studied adopting the $k - \omega$ SST turbulence model that showed good performance for the $\beta = 90^\circ$ case. The obtained results are judged as adequate when they are compared with experimental and numerical data for geometries $\beta = 90^\circ$ and $\beta = 60^\circ$. Furthermore, the CFD force coefficients are not stationary and therefore clear periodic patterns are present in the force coefficients time histories, in agreement with wind tunnel tests. These results are provided in Table 12.

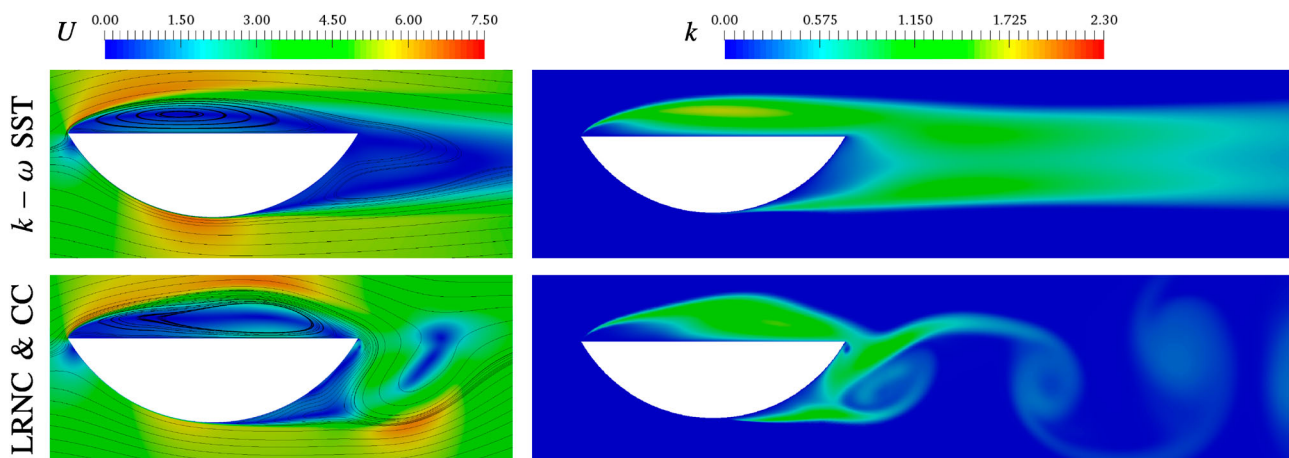


Figure 17. Flow velocity U and turbulence kinetic energy k fields obtained for $\beta = 60^\circ$ at $\alpha = 1^\circ$ using the $k - \omega$ SST turbulence model without and with low-Reynolds-number and curvature corrections. The instantaneous fields correspond to the maximum lift in the periodic time history ($\theta = \pi/2$).

Table 13. Comparison of the results for the case $\beta = 50^\circ$ for angle of attack $\alpha = 0^\circ$ using the $k - \omega$ SST turbulence model with and without low-Reynolds-number correction (LRNC) and curvature correction (CC), and Transition SST turbulence model.

Case	C_L	C_D	C_M	S_t
Expected ⁺	0.089	0.139	0.135	0.210
$k - \omega$ SST	-0.241	0.099	0.102	0.446
$\delta_{k-\omega}$ [%]	370.787	28.777	24.444	112.381
$\Delta_{k-\omega}$	0.330	0.040	0.033	0.236
LRNC	0.520	0.138	0.140	0*
$\delta_{LRNC\&CC}$ [%]	484.270	0.719	3.704	100.000
$\Delta_{LRNC\&CC}$	0.431	0.001	0.005	0.210
LRNC & CC	-0.404	0.199	0.150	0.230
$\delta_{LRNC\&CC}$ [%]	553.933	43.165	11.111	9.524
$\Delta_{LRNC\&CC}$	0.493	0.060	0.015	0.020
Transition SST	0.068	0.127	0.135	0.221
$\delta_{TransitionSST}$ [%]	23.596	8.633	0.000	5.238
$\Delta_{TransitionSST}$	0.021	0.012	0.000	0.011

*Stationary response.

+These values were obtained from the numerical estimation of the response at $\beta = 50^\circ$ provided in Figure 19. All relative and absolute errors provided in this Table are referred to these expected values.

7.5. $\beta = 50^\circ$ case

This geometry represents an intermediate case between $\beta = 60^\circ$ and $\beta = 40^\circ$ geometries that have been

previously analyzed, which showed the difficulties of the standard version of the $k - \omega$ SST turbulence model and the $k - \omega$ SST turbulence model including LRNC to properly simulate the aerodynamic responses. It has been found that in the case of the geometry $\beta = 50^\circ$ ($B/H = 4.29$, $Re_R = 0.653 \cdot 10^5$), a deeper study had to be conducted. In order to provide a set of reference values for the force coefficients and Strouhal number to validate the results obtained for this geometry, a numerical approximation considering all the results obtained in this work for each value of beta, that is reported in Figure 19, is used, giving place to $C_L \approx 0.089$, $C_D \approx 0.139$, $C_M \approx 0.135$ and $S_t \approx 0.21$. It is reported in Table 13 that the results obtained adopting the $k - \omega$ SST turbulence model without corrections and introducing LRNC and CC corrections are far from those. This is indicative of the turbulence model being unable to properly simulate the aerodynamic phenomena in this geometry. Hence, simulations were also carried out using the four-equation Transition SST turbulence model that has been developed aiming to properly simulate the transition phenomena. This model was described in Section 4.3.4, and has shown good performance in several works, for instance,

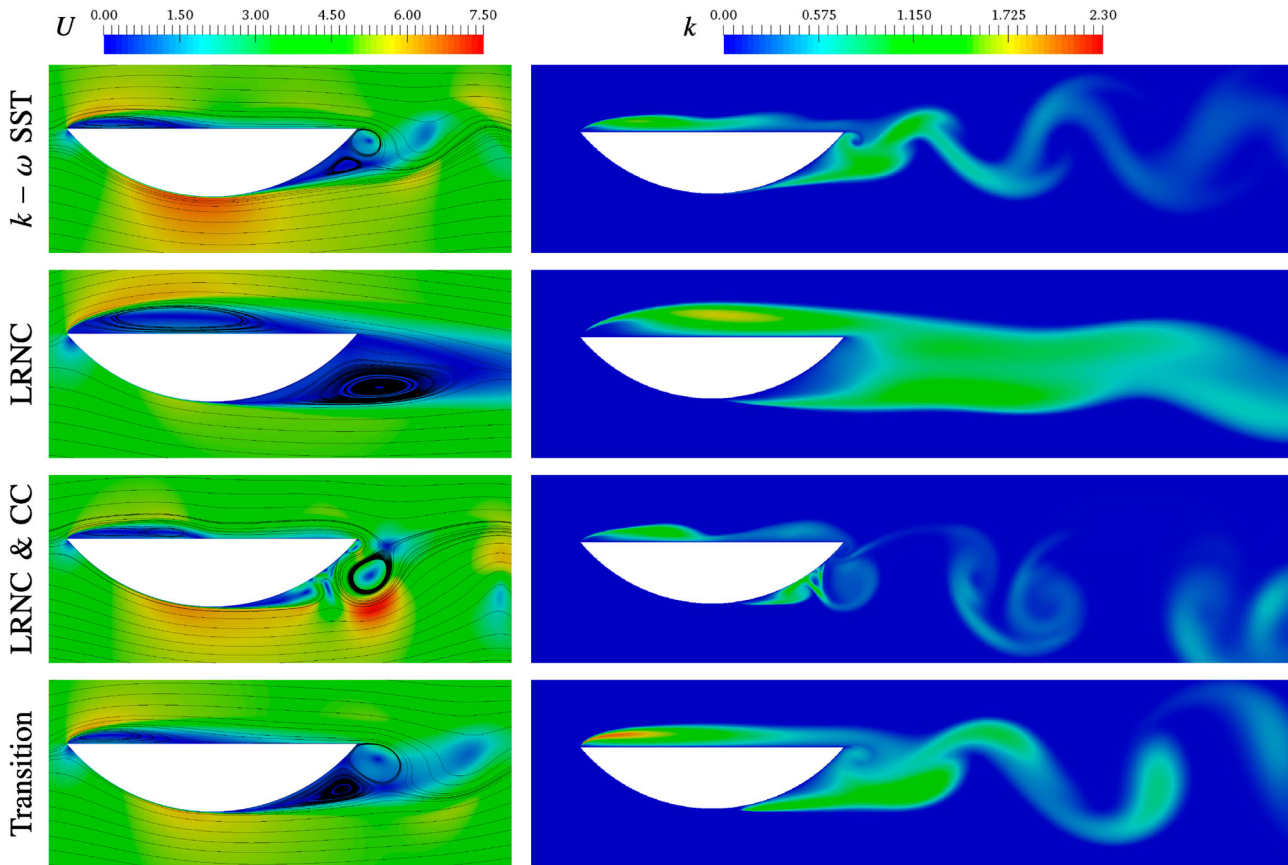


Figure 18. Flow velocity U and turbulence kinetic energy k fields obtained for $\beta = 50^\circ$ at $\alpha = 0^\circ$ using the $k - \omega$ SST turbulence model without corrections, with low-Reynolds-number corrections, with low-Reynolds-number and curvature corrections, and the Transition SST turbulence model. The instantaneous fields correspond to the maximum lift in the periodic time history ($\theta = \pi/2$).

Table 14. Comparison of the results for the section $\beta = 50^\circ$ for angle of attack $\alpha = 1^\circ$ using the $k - \omega$ SST turbulence model and Transition SST turbulence model.

Case	C_L	C_D	C_M	S_r
Expected ⁺	0.259	0.153	0.144	0.210
$k - \omega$ SST	0.025	0.098	0.123	0.015
$\delta_{k-\omega}$ [%]	90.347	35.948	14.583	92.857
$\Delta_{k-\omega}$	0.234	0.055	0.021	0.195
Transition SST	0.305	0.129	0.146	0*
$\delta_{\text{TransitionSST}}$ [%]	17.761	15.686	1.389	100.000
$\Delta_{\text{TransitionSST}}$	0.046	0.024	0.002	0.210

*Stationary response.

+These values were obtained from the numerical estimation of the response at $\beta = 50^\circ$ provided in Figure 19. All relative and absolute errors provided in this table are referred to these expected values.

in Lanzafame et al. (2014), when compared with the $k - \omega$ SST turbulence model.

It has been found (Table 13) that the use of the Transition SST turbulence model provides force coefficients and Strouhal numbers for $\alpha = 0^\circ$ with intermediate values referring to those obtained in the wind tunnel for the $\beta = 60^\circ$ and $\beta = 40^\circ$ geometries as indicated in the above paragraph (see Tables 8 and 10), which is the expected behavior for this intermediate geometry.

The flow structure provided by each turbulence model can be appreciated in Figure 18 where the instantaneous flow fields correspond to the maximum lift during one cycle of lift time history ($\theta = \pi/2$). The $k - \omega$ SST turbulence model produces a flow structure in agreement with a super-critical regime, as studied in the previous sections for $\beta = 60^\circ$ and $\beta = 40^\circ$. When the LRNC is included in the turbulence model formulation, the response obtained is stationary with a large bubble on the rectilinear side that generates an increase in the lift coefficient (see Table 13). The inclusion of the curvature correction is not capable of properly resolve the wake region and the separation from the curved side, which affects the force coefficients, increasing the C_D and providing a very low value of the C_L . Nevertheless, the four-equation Transition SST turbulence model simulates adequately the flow structure in agreement with the expected sub-critical regime (see Figures 14–16), which is reflected in the consistency of the force coefficients and Strouhal numbers provided in Table 13 when they are compared with the expected values.

For the angle of attack $\alpha = 1^\circ$, the $k - \omega$ SST turbulence model produces again the previously described anticipation of the super-critical regime, with low C_L and C_D (see Table 14), and delayed separation point on the curved side, as shown in Table 14. The transition turbulence model reproduces more accurately the sub-critical regime characteristics and offers values for the force coefficients consistent with the expected values

accordingly with the results obtained for $\beta = 40^\circ$ and $\beta = 60^\circ$. The steadiness in the flow found for the $\alpha = 1^\circ$ angle of attack may be explained by the more important relative contribution of the stochastic fluctuations, that may damp the fluctuating motion of the flow around the body as it has been analyzed in Bruno and Khris (2003) for turbulence models based on the isotropic eddy viscosity hypothesis.

7.6. Summary of the numerical results

This section summarizes the results obtained for the whole set of geometries analyzed in this work aiming to characterize the aerodynamic response of circular segments depending on their corner angle.

Figure 19 contains the whole picture of the aerodynamic responses, comparing the numerical values with the wind tunnel experimental data. In this figure, the numerical values are approximated by second-order polynomials aiming to approximate the trend of the aerodynamic response of the circular segments for corner angles in the range $\beta = [40^\circ, 90^\circ]$. These curves may be helpful for establishing at the initial design stage the static loads on structural elements with these shapes and approximating some aeroelastic responses that may be estimated by means of the force coefficients and their slopes, such as buffeting and flutter in the frame of energy harvesting studies.

The aerodynamic loads can be estimated from the information provided in Figure 19 for the mean force coefficients at $\alpha = 0^\circ$. It can be appreciated that the C_L and C_D values increase as the corner angle β grows from the $\beta = 40^\circ$ geometry to the D-section case ($\beta = 90^\circ$), since β enhances the curvature and the depth of the cross-section. Therefore, for high values of β , the lift and drag forces are high, as expected. In the case of the C_M , the behavior is different. Although this coefficient grows slightly with β in the range $\beta = [40^\circ, 60^\circ]$, for values of the corner angle higher than $\beta = 60^\circ$ the value of the moment coefficient turns nearly constant, around $C_M \approx 0.14$.

The behavior of these geometries for an angle of attack $\alpha = 1^\circ$ presents a similar trend as that shown for $\alpha = 0^\circ$ in the domain of values of β under study. In general, the values of the force coefficients for $\alpha = 1^\circ$ are higher than for $\alpha = 0^\circ$, particularly in the range $\beta = [40^\circ, 70^\circ]$, which results in positive slopes for the force coefficients. However, it can be seen that the value of the C_L at $\alpha = 1^\circ$ when $\beta > 85^\circ$ is higher than the value at $\alpha = 0^\circ$, which leads to a negative slope of the C_L . The same analysis can be made for the C_M for values of the corner angle β higher than 75° . Negative slopes for the lift and moment coefficients are related with aeroelastic instability at low flow

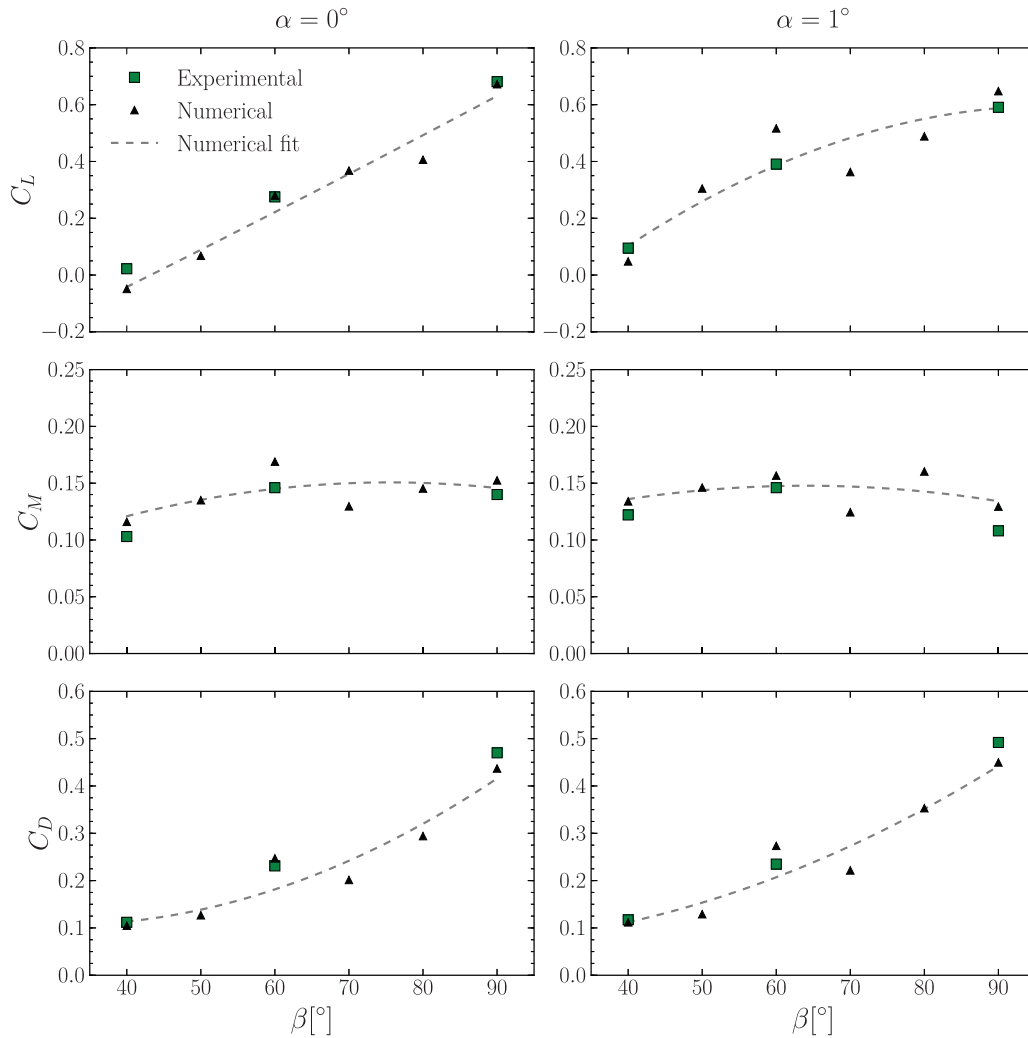


Figure 19. Comparison of the CFD and experimental results of the force coefficients in the domain $\beta = [40^\circ, 90^\circ]$ for $\alpha = 0^\circ$ and $\alpha = 1^\circ$. The numerical results reported herein were obtained with the use of the most adequate turbulence model in each case.

speed, which is of utmost interest in energy harvesting applications.

The trend in the force coefficients and slopes as a function of the shape of a generic cross-section can be useful when considering shape variations in the design of buildings, footbridges or bridges (Mou, He, Zhao, & Chau, 2017). Particularly, in Hernández, Cid, Nieto, and Jurado (2016), an optimization of a long span bridge is proposed considering variations of the shape of circular segments as the ones studied in this work. In addition, some recent references propose the shape optimization of tall buildings cross-section, such as the works by Bernardini, Spence, Wei, and Kareem (2015) and Elshaer, Bitsumlak, and El Damatty (2017), and deck cross-sections, such as Cid Montoya, Hernández, and Nieto (2018), taking advantage of the use of surrogate models. Determining the sensitivity of force coefficients with respect to shape variations of the cross-section under study is one of the current challenges in the wind engineering field.

Therefore, the study of the effects on the aerodynamic response of shape modifications in structural elements is a key aspect in the structural design field.

8. Conclusions

Circular segments are increasingly present in different engineering fields, however, the existing literature on the aerodynamic response of this type of geometry is scarce. Only the so-called ‘D-section’ (semi-circular cylinder) has traditionally attracted the attention of the research community, mainly due to its equivalence to ice-accreted conductors. Experimental-based research has focused on galloping-related studies, and the available force coefficients shown a certain scattering.

This piece of research has studied several circular segments, considering changes in the geometry from the semi-circular shape to circular segments whose behavior can be assumed to be closer to a streamlined

cross-section. The numerical simulations have been conducted using 2D URANS and several turbulence models. A number of meshes have been made for the different geometries under study, combining structured mesh regions with a non-structured buffer zone. The used CFD solvers were OpenFOAM, for the simulations where the standard version of Menter's $k - \omega$ SST turbulence model was adopted, and ANSYS, for the simulations where the LRNC and LRNC & CC versions of the $k - \omega$ SST model, and the Transition SST model, were used.

Numerical simulations of the aerodynamic response of the considered geometries present important challenges related with the correct modeling of flow separation transition and interaction between shear layers. For validation purposes, wind tunnel tests have been conducted for obtaining the Strouhal numbers and the force coefficients and their slopes for the cases $\beta = [40^\circ, 60^\circ, 90^\circ]$. Menter's $k - \omega$ SST turbulence model has provided accurate results in the range of corner angles $\beta = [70^\circ, 90^\circ]$. However, for corner angles $\beta = 60^\circ$ and $\beta = 40^\circ$, low Reynolds and curvature corrections were required in order to obtain results providing a close match with experimental data. For $\beta = 50^\circ$, the application of the four-equation Transition SST turbulence model was needed in order to obtain values for the force coefficients in agreement with the expected data for this geometry. The global consideration of the results reported herein points to the inability of the $k - \omega$ SST turbulence model to simulate transition for medium and low corner angles since the transition phenomena is not properly addressed, and the coincidental ability of corrected two-equation turbulence models to reliably simulate transition-related problems (Menter et al., 2006). The success of the transition SST model in the case where the other considered turbulence models had failed remarks its good performance in complex transition-related problems since this model specifically models transition.

The studies conducted in this work have allowed to identify the trend for the force coefficients and their slopes in terms of the shape parameter β , which is the corner angle, for two angles of attack. These studies provide information about the aerodynamic forces acting on the considered geometries, along with some insights on their aeroelastic stability and their main flow features. From the aerodynamics point of view, in general the force coefficients grow as the corner angle β increases. Regarding the aeroelastic stability, for high values of β , the slopes of the lift and moment coefficients are negative and consequently these geometries would be prone to aeroelastic excitation at low flow speeds. However, given the degree of bluntness of these geometries, proper aeroelastic analyses must be conducted to precisely identify their aeroelastic behavior.

The information provided by this study might be very useful for those involved in wind-resistant or energy-harvesting design of structural elements with cross-sections of circular segment geometry with different chord to sagitta ratios. An interesting future line of research could be the consideration of more wind angles of attack, in order to extend the aerodynamic characterization of these geometries. Also transition could be studied considering 3D geometries and Large Eddy Simulation (LES) models. This would be of utmost interest for researchers and engineers involved in both wind-resistant or energy-harvesting problems.

Disclosure statement

No potential conflict of interest was reported by the authors.

Funding

The research leading to these results has received funding from the Spanish Minister of Economy, Industry and Competitiveness (MINECO) with project reference BIA2013-41965-P. The first author have been also funded by the Fundación Pedro Barrié de la Maza and the University of La Coruña. The third author have been funded by grant BES-2014-068418. The authors fully acknowledge the support received.

ORCID

M. Cid Montoya  <http://orcid.org/0000-0002-3647-6022>

References

- Abdelkefi, A. (2016). Aeroelastic energy harvesting: A review. *International Journal of Engineering Science*, 100, 112–135.
- Abdelkefi, A., Hajj, M. R., & Nayfeh, H. (2013). Piezoelectric energy harvesting from transverse galloping of bluff bodies. *Smart Materials and Structures*, 22(1), 15014.
- Abdelkefi, A., Yan, Z., & Hajj, M. R. (2014). Performance analysis of galloping-based piezoaeroelastic energy harvesters with different cross-section geometries. *Journal of Intelligent Material Systems and Structures*, 25(2), 246–256.
- Achenbach, E., & Heinecke, E. (1981). On the vortex shedding from smooth and rough cylinders in the range of Reynolds numbers 6×10^3 to 5×10^6 . *Journal of Fluid Mechanics*, 109, 239–251.
- Ahmad, N. N., Proctor, F. H., & Perry, R. B. (2013). *Numerical simulation of the aircraft wake vortex flowfield*. Proceeding of 5th AIAA Atmospheric and Space Environments Conference, San Diego, CA.
- Algaard, W. H., Lewis, J. E., Lang, B., & Johnson, A. (2010). *The Nichols bridge at the art institute of Chicago*. Proceedings of the 2010 ASCE Structures Congress, Orlando, FL (pp. 238–249).
- Ali, M., Arafa, M., & Elaraby, M. (2013). *Harvesting energy from galloping oscillations*. Proceedings of the World Congress on Engineering, WCE 2013, London.
- Anderson, J. D. (1995). *Computational fluid dynamics: The basics with applications*. New York, NY: McGraw-Hill.
- Ansys fluent theory guide. (2013). *Computer software manual*. Canonsburg, PA.

- Barrero-Gil, A., Alonso, G., & Sanz-Andres, A. (2010). Energy harvesting from transverse galloping. *Journal of Sound and Vibration*, 329, 2873–2883.
- Bearman, P. (1997). Near wake flows behind two- and three-dimensional bluff bodies. *Journal of Wind Engineering and Industrial Aerodynamics*, 69–71, 33–54.
- Bernardini, E., Spence, S. M. J., Wei, D., & Kareem, A. (2015). Aerodynamic shape optimization of civil structures: A CFD-enables kriging-based approach. *Journal of Wind Engineering and Industrial Aerodynamics*, 144, 154–164.
- Blevins, R. D. (1990). *Flow-induced vibrations* (2nd ed.). New York, NY: Van Nostrand Reinhold.
- Bot, P. B., Rabaud, M., Thomas, G., Lombardi, A., & Lebre, C. (2016). Sharp transition in the lift force of a fluid flowing past nonsymmetrical obstacles: Evidence for a lift crisis in the drag crisis regime. *Physical Review Letters, American Physical Society*, 117(23), 234501.
- Bruno, L., Coste, N., & Fransos, D. (2012). Simulated flow around a rectangular 5:1 cylinder: Spanwise discretisation effects and emerging flow features. *Journal of Wind Engineering and Industrial Aerodynamics*, 104–106, 203–215.
- Bruno, L., Fransos, D., Coste, N., & Bosco, A. (2010). 3D flow around a rectangular cylinder: A computational study. *Journal of Wind Engineering and Industrial Aerodynamics*, 98, 263–276.
- Bruno, L., & Khris, S. (2003). The validity of 2D numerical simulations of vortical structures around a bridge deck. *Mathematical and Computer Modelling*, 37, 795–828.
- Bruno, L., Salvetti, M. V., & Ricciardelli, F. (2014). Benchmark on the aerodynamics of a rectangular 5:1 cylinder: An overview after the first four years of activity. *Journal of Wind Engineering and Industrial Aerodynamics*, 126, 87–106.
- Brusiani, F., de Miranda, S., Patruno, L., Ubertini, F., & Vaona, P. (2013). On the evaluation of bridge deck flutter derivatives using RANS turbulence models. *Journal of Wind Engineering and Industrial Aerodynamics*, 119, 39–47.
- Caracoglia, L., Sarkar, P. P., Haan, F. L., Sato, H., & Murakoshi, J. (2009). Comparative and sensitivity study of flutter derivatives of selected bridge deck sections, Part 2: Applications on the aerodynamic stability of long-span bridges. *Engineering Structures*, 31, 2194–2202.
- Cheers, F. (1950). *A note on galloping conductors* (Tech. Rep. No. MT-14). National Research Council of Canada.
- Chen, X. Y., Wang, B., Zhu, L. D., & Li, Y. L. (2018). Numerical study on surface distributed vortex-induced force on a flat-steel-box girder. *Engineering Applications of Computational Fluid Mechanics*, 12, 41–56.
- Choi, H., Jeon, W. P., & Kim, J. (2008). Control of flow over a bluff body. *Annual Review of Fluid Mechanics*, 40(1), 113–139.
- Cid Montoya, M., Hernández, S., & Nieto, F. (2018). Shape optimization of streamlined decks of cable-stayed bridges considering aeroelastic and structural constraints. *Journal of Wind Engineering and Industrial Aerodynamics*, 177, 429–455.
- Cid Montoya, M., Nieto, F., Hernández, S., Kusano, I., Álvarez, A. J., & J. Á. Jurado (2018). CFD-based aeroelastic characterization of streamlined bridge deck cross-sections subject to shape modifications using surrogate models. *Journal of Wind Engineering and Industrial Aerodynamics*, 177, 405–428.
- Coleman, H. S., & Steele, W. G. (2009). *Experimentation, validation, and uncertainty analysis for engineers* (3rd ed.). Hoboken, NJ: John Wiley & Sons.
- Collie, S., Gerritsen, M., & Jackson, P. (2008). Performance of two-equation turbulence models for flat plate flows with leading edge bubbles. *Journal of Fluids Engineering*, 130, 02120111.
- Da Soghe, R., Innocenti, L., Andreini, A., & Poncet, S. (2010). *Numerical benchmark of turbulence modelling in gas turbine rotor-stator system*. ASME turbo expo 2010: Power for land, sea & air (gt2010).
- Davenport, A. G. (1983). The relationship of reliability to wind loading. *Journal of Wind Engineering and Industrial Aerodynamics*, 13, 3–27.
- de Miranda, S., Patruno, L., Ubertini, F., & Vairo, G. (2014). On the identification of flutter derivatives of bridge decks via RANS turbulence models: Benchmarking on rectangular prisms. *Engineering Structures*, 76, 359–370.
- Den Hartog, J. P. (1932). Transmission line vibration due to sleet. *AIEE – American Institute of Electrical Engineers Transactions*, 51, 1074–1086.
- Dhokal, T. P., & Walters, D. K. (2011). A three-equation variant of the sst k-x model sensitized to rotation and curvature effects. *Journal of Fluids Engineering*, 133, 111201.
- Di Pasquale, D., Rona, A., & Garrett, S. J. (2009). *A selective review of CFD transition models*. 39th AIAA Fluid Dynamics Conference, San Antonio, TX.
- Elshaer, A., Bitsuamlak, G., & El Damatty, A. (2017). Enhancing wind performance of tall buildings using corner aerodynamic optimization. *Engineering Structures*, 136, 133–148.
- Fransos, D., & Bruno, L. (2010). Edge degree-of-sharpness and free-stream turbulence scale effects on the aerodynamics of a bridge deck. *Journal of Wind Engineering and Industrial Aerodynamics*, 98, 661–671.
- Ghahremanian, S., & Moshfegh, B. (2014). Evaluation of Rans models in predicting low Reynolds, free, turbulent round jet. *Journal of Fluids Engineering, ASME*, 136(1), 011201.
- Grabe, C. (2013). Correlation-based transition transport modeling for three-dimensional aerodynamic configurations. *Journal of Aircraft*, 50(5), 1533–1539.
- Guerrero, J. (2013). *Introductory OpenFOAM course*. University of Genoa, Dipartimento di Ingegneria Civile, Chimica e Ambientale (DICCA).
- Harris, C. O. (1949). *Galloping conductors* (Tech. Rep. No. Second report on a Utilities Research Commission Project). Department of Engineering Mechanics, University of Notre Dame.
- Hernández, S. (1998). *Some experiences in girder and arch bridges in Spain*. Fifth international conference on Short and Medium Span Bridges, Calgary, Alberta, Canada.
- Hernández, S., Cid, M., Nieto, F., & Jurado, J. A. (2016). *Optimization of stays and deck shape in cable supported bridges including structural and aeroelastic constraints*. 8th international colloquium on Bluff Body Aerodynamics and Applications, Boston, MA.
- Hofmann, H. M., Kaiser, R., Kind, M., & Martin, H. (2007). Calculations of steady and pulsating impinging jets – an assessment of 13 widely used turbulence models. *Numerical Heat Transfer, Part B*, 51, 565–583.
- Holden, D., Socha, J. J., Cardwell, N. D., & Vlachos, P. P. (2014). Aerodynamics of the flying snake *chrysopelea paradisi*: How

- a bluff body cross-sectional shape contributes to gliding performance. *Journal of Experimental Biology*, 217(3), 382–394.
- Holmes, J. (2015). *Wind loading of structures* (3rd ed.). Boca Raton, FL: CRC Press.
- Jones, W. P., & Launder, B. E. (1972). The prediction of laminarization with a two-equations model of turbulence. *International Journal of Heat and Mass Transfer*, 15, 301–314.
- Kareem, A. (1988). Effect of parametric uncertainties on wind excited structural response. *Journal of Wind Engineering and Industrial Aerodynamics*, 30, 233–241.
- Kwok, K. C. S. (1986). Turbulence effect on flow around circular cylinder. *Journal of Engineering Mechanics*, 112(11), 1181–1197.
- Lanchester, F. W. (1907). *Aerodynamics*. London: Constable.
- Langtry, R. B., & Menter, F. R. (2009). Correlation-based transition modeling for unstructured parallelized fluid dynamic codes. *AIAA Journal*, 47, 2894–2906.
- Langtry, R. B., Menter, F. R., Likki, S. R., Suzen, Y. B., Huang, P. G., & Völker, V. (2006). A correlation-based transition model using local variables – part II: Test cases and industrial applications. *Journal of Turbomachinery*, 128, 423–434.
- Lanzafame, R., Mauro, S., & Messina, M. (2014). 2d CFD modeling of h-Darrieus wind turbines using a transition turbulence model. *Energy Procedia*, 45, 131–140.
- Launder, B. E., & Sharma, B. I. (1974). Application of the energy-dissipation model of turbulence to the calculation of flow near a spinning disc. *Letters in Heat and Mass Transfer*, 1(2), 131–137.
- Mannini, C., Soda, A., & Schewe, G. (2010). Unsteady RANS modeling of flow past a rectangular cylinder: Investigation of Reynolds number effects. *Computers & Fluids*, 39, 1609–1624.
- Mannini, C., Šoda, A., Voß, R., & Schewe, G. (2010). Unsteady RANS simulations of flow around a bridge section. *Journal of Wind Engineering and Industrial Aerodynamics*, 98, 742–753.
- Mariotti, A., Salvetti, M. V., Shoeibi Omrani, P., & Witteveen, J. A. S. (2016). Stochastic analysis of the impact of freestream conditions on the aerodynamics of a rectangular 5:1 cylinder. *Computers and Fluids*, 136, 170–192.
- Maruai, N. M., Ali, M. S. M., Ismail, M. H., & Zaki, S. A. (2018). Flow-induced vibration of a square cylinder and downstream flat plate associated with micro-scale energy harvester. *Journal of Wind Engineering and Industrial Aerodynamics*, 175, 264–282.
- Menter, F. R. (1993). *Zonal two equation k-omega turbulence models for aerodynamic flows*. 24th AIAA Fluid Dynamics Conference; AIAA 93-2906, Orlando, FL.
- Menter, F. R. (1994). Two-equation eddy-viscosity turbulence models for engineering applications. *AIAA Journal*, 32(8), 1598–1605.
- Menter, F., & Esch, T. (2001). *Elements of industrial heat transfer prediction*. Sixteenth Brazilian congress of Mechanical Engineering, Uberlândia, Minas Gerais, Brasil.
- Menter, F. R., Kuntz, M., & Langtry, R. (2003). Ten years of industrial experience with the SST turbulence model. In *Turbulence, heat and mass transfer* (vol. 4, pp. 625–632). Redding, CT: Begell House.
- Menter, F. R., Langtry, R. B., Likki, S. R., Suzen, Y. B., Huang, P. G., & Völker, S. (2006). A correlation-based transition model using local variables – Part I: Model formulation. *Journal of Turbomachinery (ASME)*, 128, 413–422.
- Miklasz, K., LaBarbera, M., Chen, X., & Socha, J. J. (2010). Effects of body cross-sectional shape on flying snake aerodynamics. *Experimental Mechanics*, 50(9), 1335–1348.
- Mou, B., He, B. J., Zhao, D. X., & Chau, K. W. (2017). Numerical simulation of the effects of building dimensional variation on wind pressure distribution. *Engineering Applications of Computational Fluid Mechanics*, 11(1), 293–309.
- Naudascher, E., & Rockwell, D. (1994). *Flow-induced vibrations: An engineering guide*. Rotterdam: A. A. Balkema.
- Nieto, F., Hargreaves, D. M., Owen, J. S., & Hernández, S. (2015). On the applicability of 2D URANS and SST $k - \omega$ turbulence model to the fluid-structure interaction of rectangular cylinders. *Engineering Applications of Computational Fluid Mechanics*, 9(1), 157–173.
- Nieto, F., Hernández, S., Jurado, J. A., & Baldomir, A. (2010). CFD practical application in conceptual design of a 425 m cable-stayed bridge. *Wind and Structures*, 13(4), 309–326.
- Nieto, F., Hernández, S., Kusano, I., & Jurado, J. A. (2012). *CFD aerodynamic assessment of deck alternatives for a cable-stayed bridge*. Seventh international colloquium on Bluff Body Aerodynamics and Applications, Shanghai, China.
- Nieto, F., Kusano, I., Hernández, S., & Jurado, J. A. (2010). *CFD analysis of the vortex-shedding response of a twin-box deck cable-stayed bridge*. Fifth international symposium on Computational wind Engineering, Chapel Hill, NC.
- Nieto, F., Owen, J. S., Hargreaves, D. M., & Hernández, S. (2015). Bridge deck flutter derivatives: Efficient numerical evaluation exploiting their interdependence. *Journal of Wind Engineering and Industrial Aerodynamics*, 136, 138–150.
- Nikitas, N., & Macdonald, H. G. (2014). Misconceptions and generalizations of the den Hartog galloping criterion. *Journal of Engineering Mechanics*, 140, 04013005.
- Novak, M., & Tanaka, H. (1974). Effect of turbulence on galloping instability. *Journal of the Engineering Mechanics Division*, 100(1), 27–47.
- Openfoam user guide. (2015). *Computer software manual*.
- Pantaleón, M. J., Revilla, R., & Olazábal, P. (2014). Santander Bay's Footbridge. *Structural Engineering International*, 24(1), 96–97.
- Parkinson, G. V., & Brooks, N. P. H. (1961). On the aeroelastic instability of bluff cylinders. *Journal of Applied Mechanics*, 28, 252–258.
- Patruno, L. (2015). Accuracy of numerically evaluated flutter derivatives of bridge deck sections using RANS: Effects on the flutter onset velocity. *Engineering Structures*, 89, 49–65.
- Peak Aerials. (2016). *Bow building*. Retrieved from <http://www.peakairials.com/2016/02/21/tallest-buildings-in-calgary/>
- Pelletier, D. (2008). *DPW: Reflections from an outsider or the rans' elusive asymptotic range!* 26th AIAA applied aerodynamics conference, 18–21 August 2008, Honolulu, Hawaii.
- Ratkowski, J. J. (1963). *Experiments with galloping spans*. *IEEE Transactions on Power Apparatus and Systems*, 82(68), 661–669.
- Ricci, M., Patruno, L., de Miranda, S., & Ubertini, F. (2016). Effects of low incoming turbulence on the flow around a 5:1 rectangular cylinder at non-null-attack angle. *Mathematical Problems in Engineering*, 2016, 2302340–12.
- Richardson, A. S., & Martuccelli, J. R. (1963). *Research study on galloping of electric power transmission lines*. Conference on Wind Effects on Buildings and Structures, Teddington, Middlesex, UK.

- Roache, P. (2009). *Fundamentals of verification and validation*. Socorro, NM: Hermosa Publishers.
- Rostami, A. B., & Armandei, M. (2017). Renewable energy harvesting by vortex-induced motions: Review and benchmarking of technologiess. *Renewable and Sustainable Energy Reviews*, 70, 193–214.
- Salas, M., & Atkins, H. (2009). On problems associated with grid convergence of functionals. *Computers and Fluids*, 38, 1445–1454.
- Sarkar, P. P., Caracoglia, L., Haan, F. L., Sato, H., & Murakoshi, J. (2009). Comparative and sensitivity study of flutter derivatives of selected bridge deck sections, Part I: Analysis of inter-laboratory experimental data. *Engineering Structures*, 31, 158–169.
- Šarkić, A., Fisch, R., Höffer, R., & Bletzinger, K. U. (2012). Bridge flutter derivatives based on computed, validated pressure fields. *Journal of Wind Engineering and Industrial Aerodynamics*, 104–106, 141–151.
- Šarkić, A., Höffer, R., & Brčić, S. (2015). Numerical simulations and experimental validations of force coefficients and flutter derivatives of a bridge deck. *Journal of Wind Engineering and Industrial Aerodynamics*, 144, 172–182.
- Schewe, G. (1983). On the force fluctuations acting on a circular cylinder in crossflow from subcritical up to trans-critical Reynolds numbers. *Journal of Fluid Mechanics*, 133, 265–285.
- Schewe, G. (1986). Sensitivity of transition phenomena to small perturbations in flow around a circular cylinder. *Journal of Fluid Mechanics*, 172, 33–46.
- Schewe, G. (2001). Reynolds-number effects in flow around more-or-less bluff bodies. *Journal of Wind Engineering and Industrial Aerodynamics*, 89, 1267–1289.
- Schewe, G., & Larsen, A. (1998). Reynolds number effects in the flow around a bluff bridge deck cross section. *Journal of Wind Engineering and Industrial Aerodynamics*, 74–76, 829–838.
- Shimada, K., & Ishihara, T. (2002). Application of a modified $k-\epsilon$ model to the prediction of aerodynamic characteristics of rectangular cross-section cylinders. *Journal of Fluids and Structures*, 16(4), 465–485.
- Shur, M. L., Strelets, M. K., & Travin, A. K. (2000). Turbulence modeling in rotational and curved channels: Assessing the Spalart–Shur correction. *AIAA Journal*, 38, 784–792.
- Singh, S. P., & Mittal, S. (2005). Flow past a cylinder: Shear layer instability and drag crisis. *International Journal for Numerical Methods in Fluids*, 47, 75–98.
- Sirohi, J., & Mahadik, R. (2012). Harvesting wind energy using a galloping piezoelectric beam. *Journal of Vibration and Acoustics*, 134(1), 11009.
- Smirnov, P. E., & Menter, F. R. (2008). *Sensitization of the SST turbulence model to rotation and curvature by applying the Spalart–Shur correction term*. Asme paper gt 1008-50480, Berlin, Germany.
- Smirnov, P. E., & Menter, F. R. (2009). Sensitization of the SST turbulence model to rotation and curvature by applying the Spalart–Shur correction term. *Journal of Turbomachinery*, 131(4), 41010.
- Sohankar, A. (2008). Large eddy simulation of flow past rectangular-section cylinders: Side ratio effects. *Journal of Wind Engineering and Industrial Aerodynamics*, 96, 640–655.
- Spalart, P. R., & Allmaras, S. R. (1994). One-equation turbulence model for aerodynamic flows. *Recherche Aerospaciale*, 1, 5–21.
- Spalart, P. R., & Shur, M. (1997). On the sensitization of turbulence models to rotation and curvature. *Aerospace Science and Technology*, 5, 297–302.
- Stapleton, M. (2017). *The bow building*. Retrieved from <http://www.the-bow.com/>
- Sumner, D. (2010). Two circular cylinders in cross-flow: A review. *Journal of Fluids and Structures*, 26(6), 849–899.
- Sun, D., Owen, J. S., & Wright, N. G. (2009). Application of the $k-\omega$ turbulence model for a wind-induced vibration study of 2D bluff bodies. *Journal of Wind Engineering and Industrial Aerodynamics*, 97, 77–87.
- Tamura, T., & Miyagi, T. (1999). The effect of turbulence on aerodynamic forces on a square cylinder with various corner shapes. *Journal of Wind Engineering and Industrial Aerodynamics*, 83, 135–145.
- Tao, R., Xiao, R., Yang, W., & Wang, F. (2014). A comparative assessment of Spalart–Shur rotation/curvature correction in rans simulations in a centrifugal pump impeller. *Mathematical Problems in Engineering*, 2014, 342905.
- Tucker, P. (2013). Trends in turbomachinery turbulence treatments. *Progress in Aerospace Sciences*, 63, 1–32.
- Vairo, G. (2003). A numerical model for wind loads simulation on long-span bridges. *Simulation Modelling Practice and Theory*, 11(5–6), 315–351.
- Van Dyke, M. D. (1982). *An album of fluid motion*. Stanford, CA: Parabolic Press.
- Versteeg, H. K., & Malalasekera, W. (2007). *An introduction to computational fluid dynamics: The finite volume method* (2nd ed.). Harlow: Pearson Education.
- Viegas, J. R., & Rubesin, M. W. (1983). Wall-function boundary conditions in the solution of the Navier–Stokes equations for complex compressible flows. *AIAA Journal*, 83, 1694.
- Villalpando, F., Reggio, M., & Ilincă, A. (2012). Numerical study of flow around iced wind turbine airfoil. *Engineering Applications of Computational Fluid Mechanics*, 6(1), 39–45.
- Weaver, D., & Veljkovic, I. (2005). Vortex shedding and galloping of open semi-circular and parabolic cylinders in cross-flow. *Journal of Fluids and Structures*, 21, 65–74.
- Wilcox, D. C. (1988). Reassessment of the scale-determining equation for advanced turbulence models. *AIAA Journal*, 26(11), 1299–1310.
- Wilcox, D. C. (1992). *The remarkable ability of turbulence model equations to describe transition*. Fifth symposium on Numerical and Physical Aspects of Aerodynamic Flows, Long Beach, CA.
- Wilcox, D. C. (1993). Comparison of two-equation turbulence models for boundary layers with pressure gradient. *AIAA Journal*, 31(8), 1414–1421.
- Wilcox, D. C. (2005). *Elements of fluids mechanics*. La Cañada, CA: DCW Industries.
- Wilcox, D. C. (2006). *Turbulence modeling for CFD* (3rd ed.). La Cañada, CA: DCW Industries.
- Wilcox, D. C. (2011). *Basic fluid mechanics* (5th ed.). La Cañada, CA: DCW Industries.
- Williamson, C. H. K. (1996). Vortex dynamics in the cylinder wake. *Annual Review of Fluid Mechanics*, 28(1), 477–539.
- Winnipeg Architecture Foundation. (2017). *Esplanade riel pedestrian bridge – Canada*. Retrieved from <http://www.winnipegarchitecture.ca/esplanade-riel/>
- Xu, Y. L. (2013). *Wind effects on cable-supported bridges*. Singapore: John Wiley & Sons.

- Yakhot, V., & Orszag, S. A. (1986). Renormalization group analysis of turbulence: Basic theory. *Journal of Scientific Computing*, 1, 3–11.
- Zdravkovich, M. M. (1997). *Flow around circular cylinders, Vol 1: Fundamentals*. Oxford: Oxford University Press.
- Zdravkovich, M. M. (2003). *Flow around circular cylinders, Vol 2: Applications*. Oxford: Oxford University Press.
- Zhang, K., Katsuchi, H., Zhou, D., Yamada, H., & Han, Z. (2016). Numerical study on the effect of shape modification to the flow around circular cylinders. *Journal of Wind Engineering and Industrial Aerodynamics*, 152, 23–40.
- Zhang, L., & Agarwal, R. K. (2018). *Numerical simulation of flow past a circular arc and a truncated circular cylinder in transitional flow*. AIAA Scitech Forum: 2018 AIAA Aerospace Sciences Meeting, Kissimmee, FL.
- Zhang, X., Wray, T. J., & Agarwal, R. K. (2016). *Application of a new simple rotation and curvature correction to the Wray-Agarwal turbulence model*. Proceeding of 46th AIAA Fluid Dynamics Conference, Washington, DC.